https://doi.org/10.5194/egusphere-2025-772
Preprint. Discussion started: 11 June 2025

Assessment of the vulnerability of buildings destroyed during postfire debris flow events in Kule village, Yajiang County, China

Author names:

Jinshui Wang[1,2], Jiangang Chen[1,2,3*], Lu Zeng[1,2], Fei Yang[1,2], Xiao Li[1,2], Wanyu Zhao[1,2,3], Huayong Chen[1,2]

Affiliations

[1]State Key Laboratory of Natural Hazards and Engineering Safety, Institute of Mountain Hazards and Environment, Chinese Academy of Sciences, Chengdu, 610299, China;

[2]University of Chinese Academy Sciences, Beijing, 100049, China.

[3]Sichuan Province Engineering Technology Research Center of Mountain Hazards, Chengdu, 610299, China.

Corresponding author

Jiangang Chen[*]

Email: chenjg@imde.ac.cn

https://doi.org/10.5194/egusphere-2025-772
Preprint. Discussion started: 11 June 2025

Abstract

Debris flows are frequently triggered by rainstorms after wildfires and pose severe threats to the lives of downstream residents and buildings in mountainous regions. However, there has been limited focus on developing a comprehensive framework to assess the physical vulnerability of buildings to postfire debris flows. This study presents a quantitative approach for establishing a physical vulnerability model on the basis of the observed building damage features and simulated debris flow intensity values. Detailed field surveys were conducted in Kule village, Yajiang County, to analyse the characteristics of postfire debris flows and establish a building damage database. Numerical simulations using the FLO-2D model were performed to reproduce the debris flow process and quantify the debris flow intensity, including the flow depth, flow velocity, impact pressure, momentum flux, overturning moment, and relative burial height. Physical vulnerability curves were developed for brick–concrete buildings and compared with those obtained in previous studies, and the differences in vulnerability curves, intensity indicators, and functional models were examined. The results revealed that the lognormal cumulative distribution function (LNCDF) model provides the highest statistical significance in terms of the relative error and prediction accuracy. The momentum flux demonstrated greater sensitivity in distinguishing different damage categories, whereas the impact pressure provided more precise vulnerability index predictions. The proposed physical vulnerability model can be used to evaluate the structural resistance of buildings to debris flows in wildfire-affected areas, thus providing a systematic foundation for formulating risk management and mitigation strategies.

https://doi.org/10.5194/egusphere-2025-772
Preprint. Discussion started: 11 June 2025

Keywords: Postfire debris flow, Vulnerability, Building damage, Emergency evacuation

1. Introduction

Debris flows are recurring and destructive hazards in mountainous regions (Cui et al., 2018), which frequently pose a threat to downstream human lives and infrastructure, including roads, bridges, and buildings (Cui et al., 2011; Chen et al., 2021). A suitable building vulnerability assessment can provide valuable insights for risk assessment, emergency evacuation, disaster reduction and rural planning (Eidsvig et al., 2014; Zhang et al., 2018; Wang et al., 2024). Overall, in natural hazard research, vulnerability often refers to physical vulnerability (Fuchs et al., 2007), which refers to the degree of expected loss of physical structures resulting from a hazard event of a given intensity (Chen et al., 2021; Papathoma-Köhle et al., 2022). Over the past two decades, building vulnerability assessments have transitioned from qualitative approaches, such as experience- and indicator-based models, to quantitative methods, including data-driven and mechanism-based models (Luo et al., 2023). Papathoma-Köhle et al. (2017) identified three primary methods for representing physical vulnerability to debris flows: vulnerability matrices, indicators, and curves. Among these methods, vulnerability curves are widely employed to quantify the relationship between the debris flow intensity and the extent of building damage (Zhang et al., 2018; Luo et al., 2020). With increasing hazard intensity, the degree of damage follows a continuous curve (Lee et al., 2024), ranging in value from 0 (no damage) to 1 (complete damage), as determined via the data-driven approach. Several statistical method-based studies have been conducted to develop physical vulnerability curves for debris flows on the basis of field data (Lee et al., 2024). Fuchs

https://doi.org/10.5194/egusphere-2025-772
Preprint. Discussion started: 11 June 2025

et al. (2007) established a vulnerability curve for brick–concrete (BC) buildings to describe the relationship between the degree of damage and the debris flow intensity, which has been documented extensively. Moreover, Totschnig et al. (2011) studied three debris flow events and established vulnerability curves on the basis of the damage ratio of the flow depth to the building height. Kang and Kim (2016) developed vulnerability functions for different building structure types in Korea, including reinforced concrete (RC) and non-RC structures.

However, in many regions, the availability of debris flow data is often limited because of the infrequent occurrence of significant debris flow events (Navratil et al., 2013; Wang et al., 2024). Moreover, although valuable debris flow intensity-related data are regularly collected (Marchi et al., 2002), few studies have focused on monitoring the impact of debris flows on buildings (Jakob et al., 2012). Therefore, dynamic numerical models have increasingly been employed to reconstruct debris flow processes and determine the hazard intensity (Zhang et al., 2018; Ouyang et al., 2019; Chang et al. 2020; Chen et al., 2025). Such runout models play a critical role in bridging data gaps (Chen et al., 2021) and can serve as inputs for vulnerability functions to predict building damage (Barnhart et al., 2024). In prior studies, different numerical simulation models have been used to develop vulnerability curves and evaluate building failure modes (Luo et al., 2023). Lee et al. (2024) proposed a vulnerability curve of the impact pressure for brick masonry buildings in South Korea via the use of Flow-R simulation software. Barnhart et al. (2024) compared the effectiveness levels of two hazard intensity indicators (the flow depth and the momentum flux) alongside three runout models (the Rapid Mass Movement Simulation (RAMMS), FLO-2D, and D-Claw models) and applied them to obtain probabilistic forecasts

https://doi.org/10.5194/egusphere-2025-772
Preprint. Discussion started: 11 June 2025

of wood-framed building damage. Each numerical model exhibits unique advantages and tailored applications, with the FLO-2D model as the most frequently utilized option (Quan Luna et al., 2011; Zhang et al., 2018, Chen et al., 2021; Wang et al., 2024). Specifically, Quan Luna et al. (2011) developed vulnerability curves for the flow depth and impact pressure using the FLO-2D model. Zhang et al. (2018) established six vulnerability curves via FLO-2D numerical modelling, including the flow depth, flow velocity, impact pressure, momentum flux, overturning moment, and relative intensity, to assess debris flow-induced damage to BC and RC buildings in Zhouqu County, China. Chen et al. (2021) proposed a momentum flux curve for masonry wood and BC buildings in Cutou Gully, Wenchuan County, China, on the basis of FLO-2D simulations of debris flows. Wang et al. (2024) developed vulnerability curves for the flow depth and impact pressure using FLO-2D model simulations suitable for the Wangzhuangwu watershed, Zhejiang Province, China. Notably, the accuracy of this numerical model highly depends on the selection of parameter values (Chen et al., 2021), which requires a comprehensive understanding of debris flow properties, including their formation mechanisms, frequency, and intensity (Chang et al., 2020). Furthermore, accurately calculating the debris flow volume (Barnhart et al., 2024) and the peak discharge (Wang et al., 2024) is critical for ensuring the reliability of runoff dynamics prediction outcomes.

In addition, the uncertainty and accuracy of vulnerability curves are affected not only by the adopted numerical model but also by the debris flow intensity and building damage attributes, as well as the statistical functional models linking the two (Luo et al., 2023; Lee et al., 2024). First, there are numerous intensity indicators, including the two easily obtained direct quantities of the flow depth and velocity (Eidsvig et al., 2014; Kang and Kim, 2016;), as well as derivative quantities, such as the impact pressure (Quan Luna et al., 2011; Lee et al., 2024; Wang et al., 2024), momentum flux (Jakob et al., 2012; Ouyang et al., 2019; Chen et al., 2021; Barnhart et al., 2024), overturning moment (Zhang et al., 2018), and relative burial height (Totschnig et al., 2011; Zhang et al., 2018). Second, various factors related to buildings can significantly influence vulnerability assessments, including building features such as the number of floors, direction, shielding effects and construction codes (Luo et al., 2020), as well as the building structure type such as wood-frame buildings, masonry buildings, BC buildings, and RC buildings, which have been studied extensively (Lee et al., 2024). Additionally, building damage due to debris flows has been primarily classified qualitatively (Hu et al., 2012). Within this framework, the damage state is commonly categorized as slight, moderate, extensive, and complete damage (Luo et al., 2023). Third, vulnerability curves can be fitted using several functional models (Luo et al., 2023), such as polynomial functions, logistic functions, Weibull distributions, exponential functions, lognormal cumulative distribution function (LNCDF) and Avrami functions (Fuchs et al. 2007; Quan Luna et al., 2011; Eidsvig et al., 2014; Luo et al., 2023; Lee et al., 2024). Thus, further research remains needed to determine the most reliable predictions on the basis of different vulnerability functions and hazard intensity measures.

Recently, debris flow disasters after wildfires have received widespread attention, thus prompting a surge in global research on postfire hazard assessment (Kean et al., 2019; Thomas et al., 2023; Ouyang et al., 2023; He et al., 2024; Gorr et al., 2024). In steep catchments with moderate to high burn severity levels, wildfires significantly reduce vegetation cover (Rengers

https://doi.org/10.5194/egusphere-2025-772
Preprint. Discussion started: 11 June 2025

et al., 2023) and alter surface soil–hydrologic functioning (Vahedifard et al., 2024; McGuire et al., 2024). These changes render burned watersheds more susceptible than unburned watersheds to the occurrence of postfire debris flows triggered by lowering rainfall thresholds and increasing rainfall sensitivity levels (Thomas et al., 2023; Ouyang et al., 2023). Moreover, debris flows can continue to occur for years or even decades after wildfire occurrence, although triggering mechanisms and thresholds may shift (Vahedifard et al., 2024). In addition to increasing debris flow activity, burned waterslheds can generate larger-scale debris flows than unburned watersheds can (Gorr et al., 2023), resulting in greater threats to downstream lives and buildings. For example, a postfire debris flow event in Montecito, California, in January 2018 caused 23 fatalities and resulted in damage to more than 400 buildings (Kean et al., 2019). Similarly, a postfire debris flow event in the Xiangjiao catchment, Muli County, China, on 5 July 2021 destroyed 186 houses (Ouyang et al., 2023). However, more future research is needed to assess the vulnerability of buildings to postfire debris flows (Kean et al., 2019).

On March 15, 2024, a wildfire occurred in Yajiang County, Sichuan Province, China, thereby burning an area of 278.8 km^2. After the wildfire, 62 rainfall-induced debris flow events ensued in the affected area (He et al., 2024). Notably, on 10 May 2024, a postfire debris flow in Kule village, Yajiang County, China, destroyed 36 houses, blocked roads and rivers, and impacted more than half of the village residents. This event provides us with a valuable opportunity to collect postfire debris flow data and building damage data, which can enhance the assessment of building vulnerability and inform disaster reduction efforts (Zhang et al., 2018; Gorr et al., 2023).

https://doi.org/10.5194/egusphere-2025-772
Preprint. Discussion started: 11 June 2025

In this study, the aim was to comprehensively assess the physical vulnerability of buildings damaged during postfire debris flows in Kule village, Yajiang County. The primary objectives were as follows: (1) The characteristics of postfire debris flows were analysed, and a building damage database was established through field investigations. (2) Debris flow events were reconstructed via FLO-2D numerical simulations to determine the debris flow intensity. (3) Physical vulnerability curves were developed for BC buildings to assess the establishment and application of a vulnerability assessment model. (4) The differences in performance among various vulnerability approaches, such as existing intensity indicators, curves and function models, were compared. This work provides insights for advancing postfire debris flow assessments, improving vulnerability models, and guiding emergency evacuation efforts in this region.

2. Study area

The study area is located in Yajiang County, Sichuan Province, China. Yajiang County occurs in the southeastern part of the Qinghai–Tibet Plateau and the central segment of the Hengduan Mountains within the basin of the Yalong River (He et al., 2024). The Kule watershed (coordinates: 101°4′12.53″ E, 30°7′55.88″ N) is located in the northeastern part of Xiala town in Yajiang County, and the terrain encompasses mainly high mountains and deep canyons. The study area of the Kule watershed contains two primary gullies (G1 and G2), which converge with the main river in the downstream impact area of Kule village (Fig. 1). Kule village contains 58 households with 308 people, and the Kule River flows through the downstream alluvial fan of this village. The left and right banks of the village are impacted by the G1 and G2 gullies,

https://doi.org/10.5194/egusphere-2025-772
Preprint. Discussion started: 11 June 2025

respectively. The catchments of the G1 and G2 gullies cover areas of 1.4 and 3.5 km^2, respectively, and the terrain elevation differences range from 850~1,015 m. Geologically, the area primarily comprises Late Triassic silty slate. The bedrock is severely weathered and structurally fragmented. Within the catchment, the bedrock is overlain by Quaternary sediments that are approximately 1.0~3.0 m thick (He et al., 2024). The thin residual soil layer is susceptible to failure during periods of intense rainfall.

On March 15, 2024, a wildfire ignited in Yajiang County, burning 278.8 km^2 of mountainous forest and affecting 250 watersheds (He et al., 2024). The area with moderate–high burn levels accounts for more than 50% of the total catchment area. Several postfire debris flows occurred in the burned catchments on May 10 that were induced by rainfall events following the fire. In particular, the postfire debris flows in the G1 gully in Kule village destroyed 36 houses, blocked roads, and displaced people.

Yajiang County occurs in a subtropical monsoon climate zone, and the long-term annual precipitation ranges from 600 to 1200 mm, with precipitation mainly concentrated from June to September. Moreover, the average rainfall reaches 166.1 mm, accounting for more than 70% of the total annual precipitation. The rainstorm started at 14:00 on 10 May and lasted until 11 May, according to records from a rainfall monitoring station (coordinates: 101°1′20″ E, 30°1′57″ N). The maximum recorded hourly rainfall intensity was 6.9 mm/h, and the accumulated rainfall reached 37.8 mm (Fig. 2). Notably, the rainfall threshold of postfire debris flows is much lower than that of nonfire debris flows (Ouyang et al., 2023). In particular, low-intensity rainfall can trigger postfire debris flows in the G1 gully, and the G2 gully occurs in a state in which debris

https://doi.org/10.5194/egusphere-2025-772
Preprint. Discussion started: 11 June 2025

flows can occur at any time. Owing to wildfires, a large amount of loose material remains on hillslopes and in channels, which can provide abundant material sources for triggering debris flows (McGuire et al., 2024). Thus, debris flow activity in the G1 and G2 gullies may last longer.

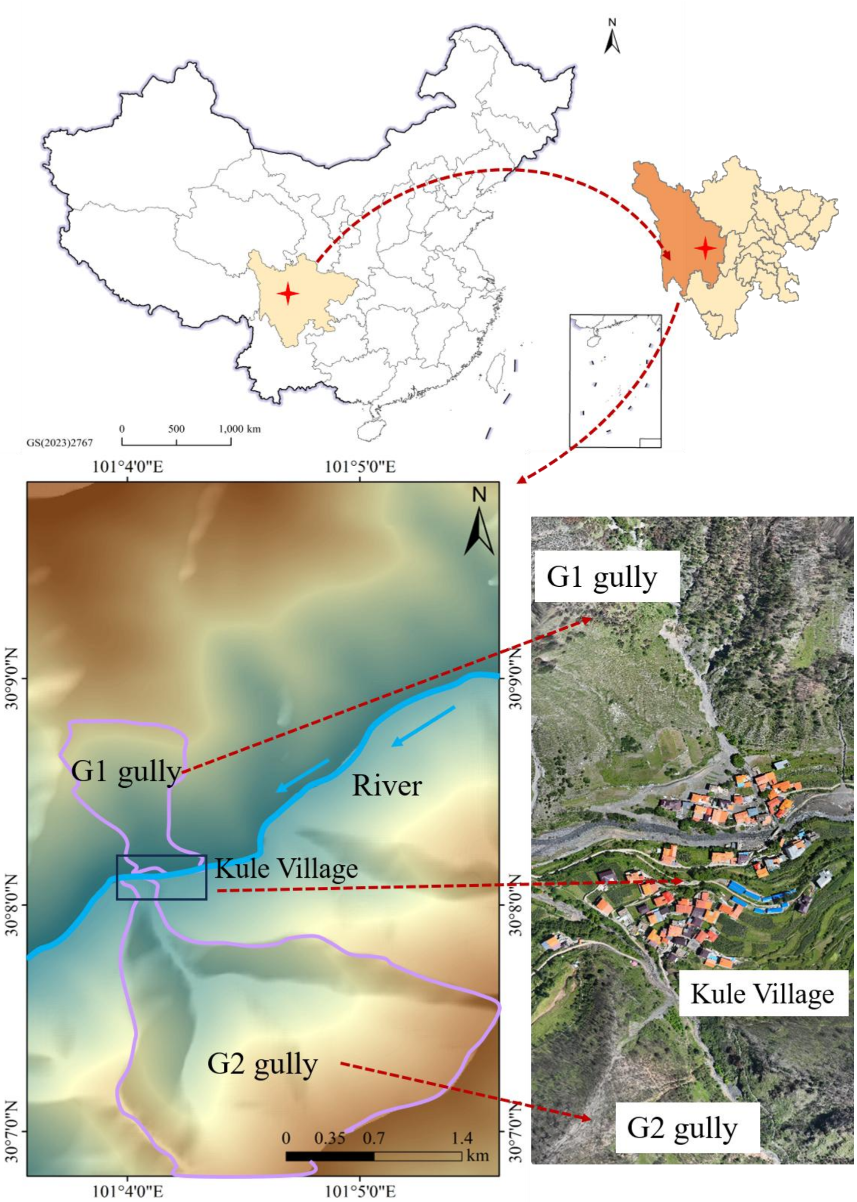

Figure 1 Location of the study area in the Kule Gully, Yajiang County, Sichuan Province, China.

https://doi.org/10.5194/egusphere-2025-772
Preprint. Discussion started: 11 June 2025

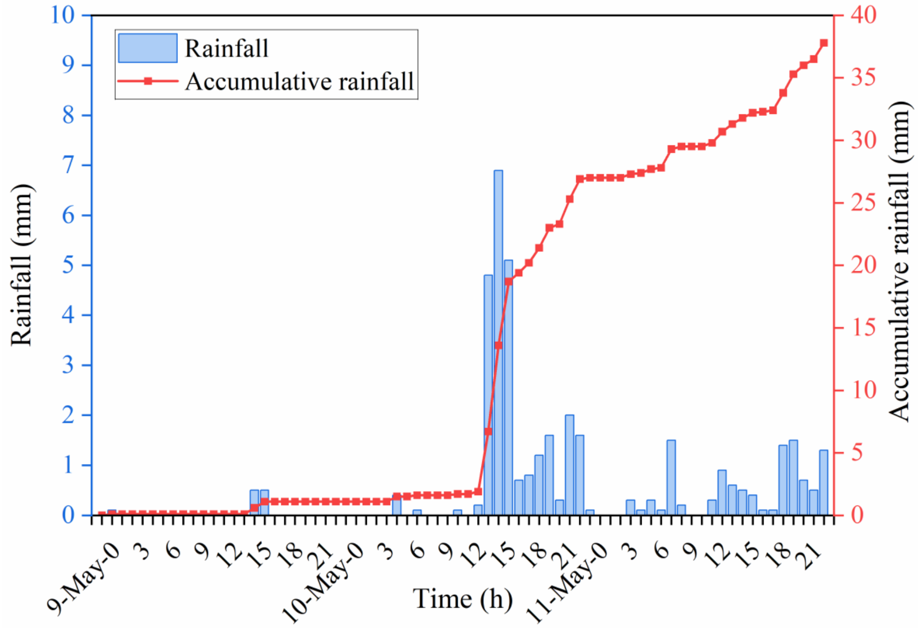

Figure 2 Hydrological characteristics: Distributions of the hourly and cumulative rainfall levels.

3. Methods

The methodological procedure in this study is divided into four steps (Fig. 3). In step 1, we conducted a field investigation and obtained images of burned areas, channel morphology, grain size distribution, and features of buildings in gullies affected by debris flows (Fig. 4). Then, we calculated the physical characteristic parameters of postfire debris flows. Finally, we reproduced and predicted dynamic runout processes via numerical simulations using the FLO-2D model. In step 2, we employed a numerical model to calculate six indicators of the debris flow intensity (Zhang et al., 2018). Moreover, the damage degree of buildings was classified, and vulnerability index values were assigned on the basis of the degree of damage to buildings (Wang et al., 2024). In step 3, we established building vulnerability curves and a function model using the reconstructed debris flow intensity and building damage information from the G1

https://doi.org/10.5194/egusphere-2025-772
Preprint. Discussion started: 11 June 2025

gully (after postfire debris flow occurrence). We subsequently applied the vulnerability model to predict potential future scenarios of building damage in the G2 gully (after postfire debris flow occurrence). Finally, in step 4, we verified and compared the performance of the proposed vulnerability model with that of previous models and provide suggestions for emergency response and evacuation routes during disasters in Kule village. This methodology facilitates a comprehensive analysis of the potential effects of future postfire debris flow events on buildings within the region, offering valuable insights for formulating disaster management and mitigation strategies.

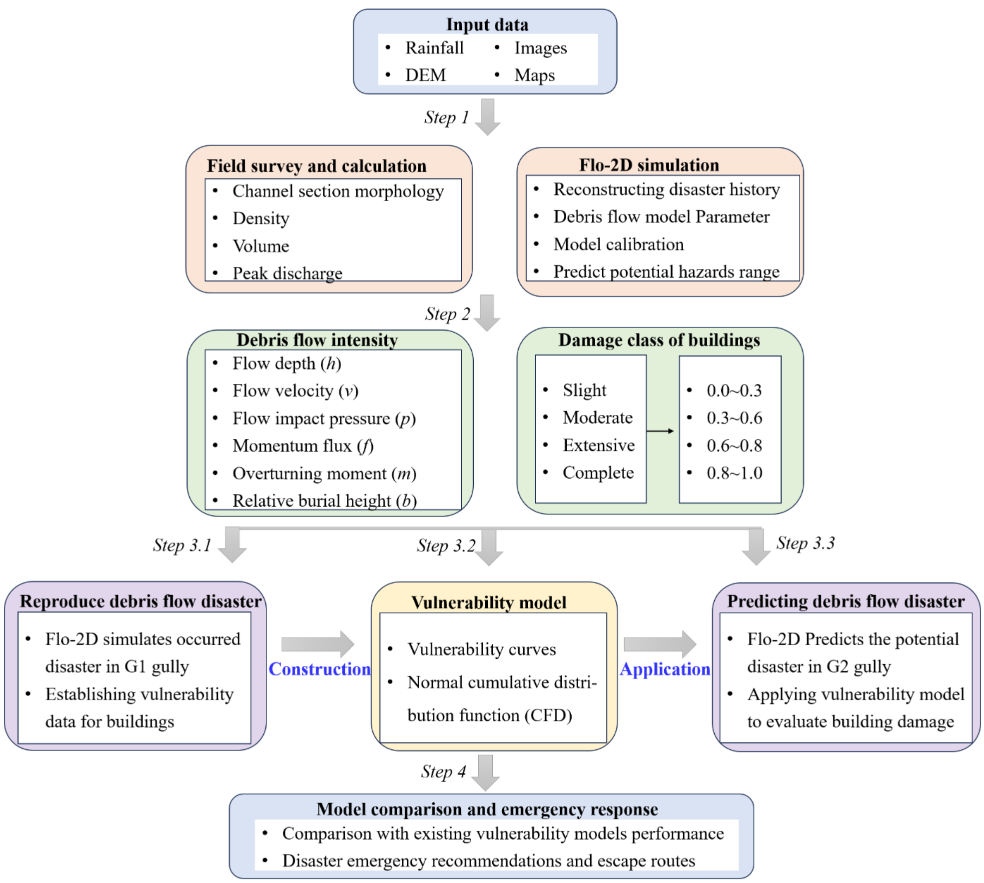

Figure 3 Methodological framework

https://doi.org/10.5194/egusphere-2025-772
Preprint. Discussion started: 11 June 2025

3.1 Field investigation

An unmanned aerial vehicle (UAV) (Inspire3, DJI-Innovations; vertical accuracy: ± 0.1 m; horizontal accuracy: ± 0.3 m) was employed to obtain images of the G1 and G2 gullies, which were used to acquire topographic and geomorphic information of channels and the spatial distribution of buildings (Fig. 5). A laser rangefinder (Contour XLRic, with a maximum range of 1,850 m and a measurement accuracy of 0.10 m) was applied to measure the dimensions of buildings (floor height, width, and length) and the section size of channels (width, gully bed gradient, and bank slope angle) (Fig. 4). The structural type, impact azimuth, affected portion and damage degree of the building were recorded with a camera (SONY A6400). The size of stone blocks, thickness of the ash layer and burned soil, burial height and flow depth mark were measured with a scale. The particle size of postfire debris flows was measured with vibrating sieving machines (measuring range: 0.25~20 mm) and Malvern particle size analysers (measuring range: 0.02–2,000 μm; scanning speed: 1,000 Hz). Then, the samples were analysed to obtain a percentage passing curve. Field work served as the basis for the subsequent simulations and the determination of postfire debris flow physical parameters.

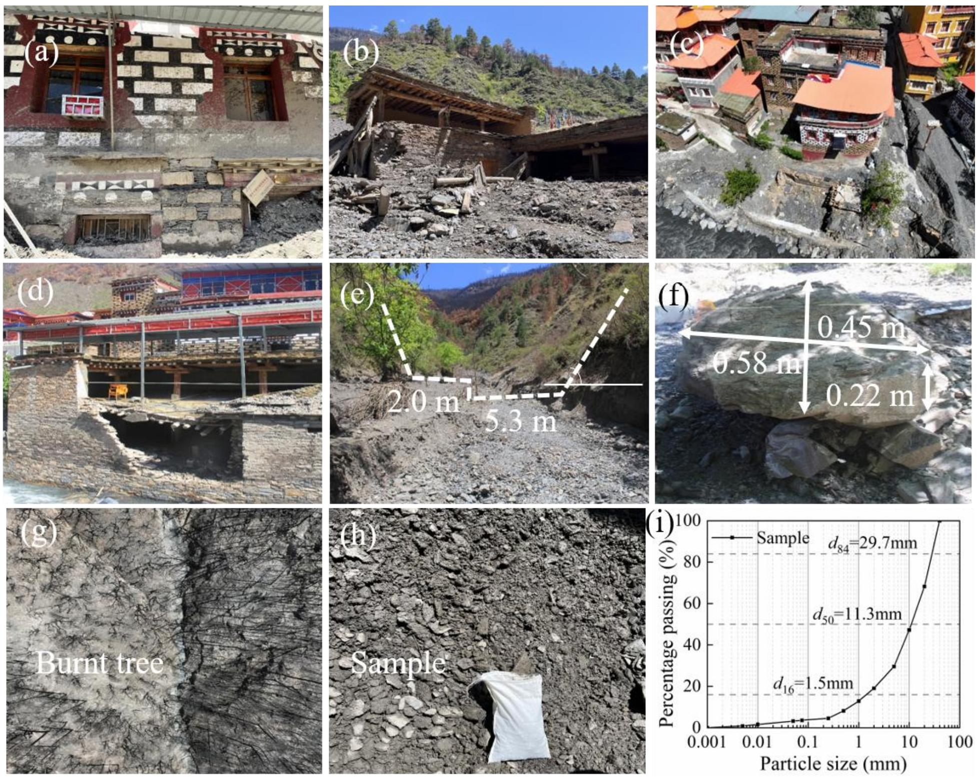

Figure 4 Fieldwork techniques for capturing postfire debris flow events: (a)–(d) Damaged buildings; (e) channel section; (f) block stone size; (g) burned area; (h) particle sampling; (i) particle size distribution curve.

The obtained aerial images were subsequently processed using PhotoScan software to generate a 3D digital orthophoto in the WGS-1984 geographic coordinate system (Wang et al. 2024) and to produce a digital elevation model (DEM), which served as base data for the subsequent runout analyses. These digital model data facilitated the identification of geomorphic features within the G1 and G2 catchments and the spatial distribution of damaged buildings (Fig. 5). The G1 and G2 gullies are located on the left and right banks of Kule village, respectively. The catchment area of the G1 gully is small, but the longitudinal gradient of the

https://doi.org/10.5194/egusphere-2025-772
Preprint. Discussion started: 11 June 2025

main channel is high, with extensive moderate–high burned areas (He et al., 2024). The catchment area of the G2 gully is large, with a lower longitudinal gradient of the main channel and a larger relative terrain elevation difference. Six cross-sectional channel measurements (from sections 1 to 6) revealed that the channel width gradually increases from upstream to downstream, ranging from 2 to 10 m (Fig. 5). The characteristic parameters of the G1 and G2 gullies are listed in Table 1.

Table 1 Characteristics of the G1 and G2 gullies on both sides of Kule village, Yajiang County

Debris flow gully	Catchment area (km^2)	Main channel length (km)	Average slope of the channel	Burned area (km^2)	Watershed relief (m)	Relative position	Debris flow event
G1 gully	1.40	1.60	0.40	0.90	850.00	Left bank of Kule village	Debris flows occurred
G2 Gully	3.50	2.20	0.17	1.50	1,015.00	Right bank of Kule village	Debris flows may occur

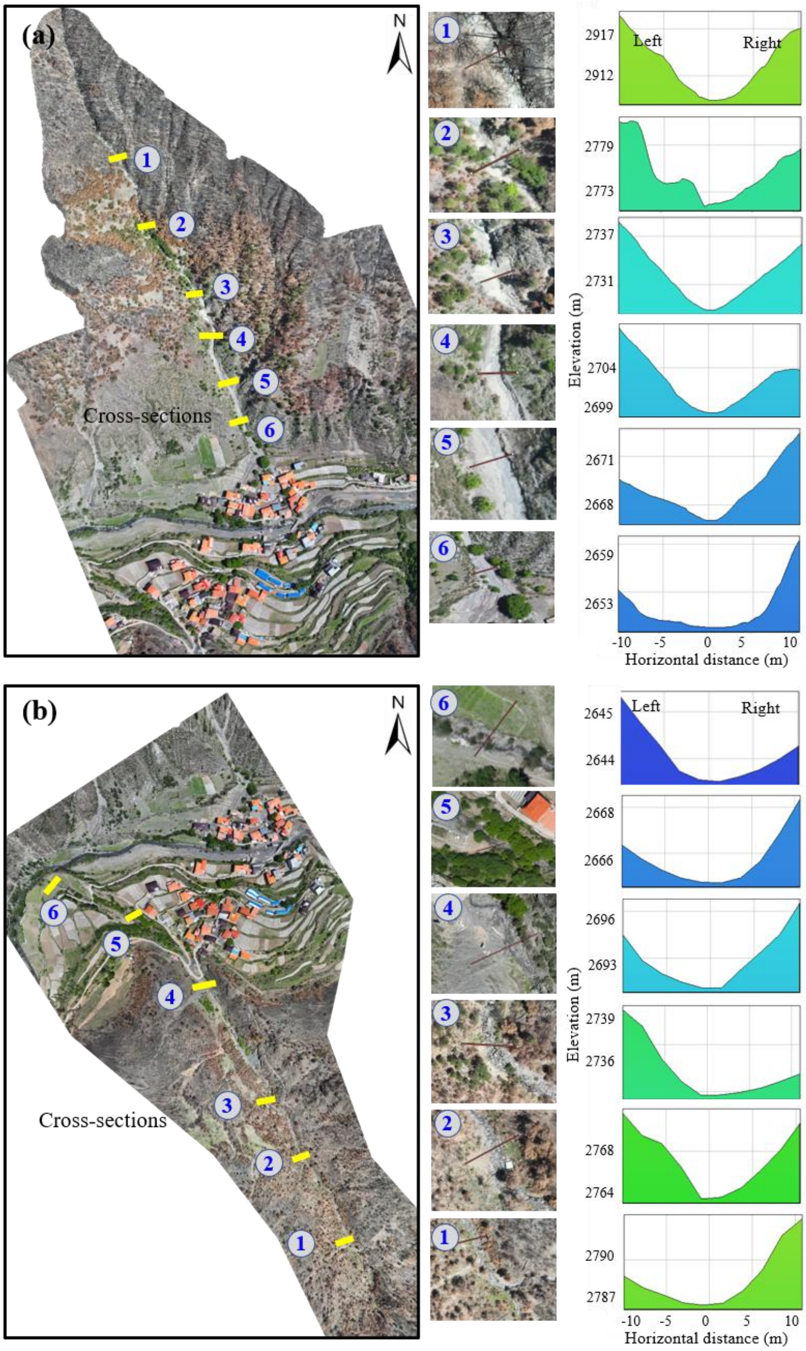

Figure 5 Characteristics of different channel cross sections: (a) G1 debris flow channel on the left bank of Kule village; (b) G2 debris flow channel on the right bank of Kule village.

https://doi.org/10.5194/egusphere-2025-772
Preprint. Discussion started: 11 June 2025

3.2 Calculation of postfire debris flow parameters

3.2.1 Debris flow density

The particle size distribution of a given debris flow deposit can be used to determine the debris flow density, which can be calculated as follows (Wang et al., 2024; Chen et al., 2021):

$$\gamma_d = \gamma_0 + \gamma_m P_2 (P_{0.05})^{0.35} \tag{1}$$

where γ_d is the density of the debris flow (g/cm^3); γ_m is the minimum density of a viscous debris flow (2.0 t/m^3); γ_0 is the minimum density of the debris flow (1.4~1.5 t/m^3); P_2 is the percentage of coarse particles with a diameter greater than 2 mm; and $P_{0.05}$ is the percentage of fine particles with a diameter smaller than 0.05 mm.

3.2.2 Debris flow volume

The US Geological Survey (USGS) debris flow hazard assessment system is based on a model developed by Gartner et al. (2014) for estimating the volume of postfire debris flows. The emergency assessment volume model is a multiple linear regression model and has been widely applied (Rengers et al., 2023; Gorr et al., 2024). This model can be expressed as follows:

$$\ln(V_{DF}) = 4.22 + 0.39\sqrt{I_{15}} + 0.36\ln\left(B_{\mathrm{mh}}\right) + 0.13\sqrt{R} \tag{2}$$

where V_{DF} is the postfire debris flow volume (m^3); I_{15} is the 15-min maximum rainfall intensity (mmh^{-1}); B_{mh} is the burned area with moderate and high burn severity levels (km^2); and R is the watershed relief (m).

3.2.3 Debris flow peak discharge

The debris flow peak discharge can be estimated via the volume–peak discharge relationship method (Rickenmann 1999; Marchi et al., 2002) or the rain-flood method (Zhou et

https://doi.org/10.5194/egusphere-2025-772
Preprint. Discussion started: 11 June 2025

al., 1991; Cui et al., 2023).

First, the peak discharge for a given catchment can be estimated on the basis of the debris flow volume (Kang and Kim, 2016). Notably, studies have demonstrated that the debris flow volume is related to the peak discharge (Navratil et al., 2013; Cui et al., 2018; Guo et al., 2024):

$$Q_d = \alpha V_{DF}{}^{\beta} \tag{3}$$

where Q_d is the peak discharge of the debris flow (m^3/s); V_{DF} is the postfire debris flow volume (m^3), which can be calculated by Eq. (2); and α and β are fitting coefficients for different watersheds, with a specific range. Please refer to Guo et al. (2024) for further details.

Second, the rain-flood method can be used for calculating rainfall-triggered debris flows under different rainfall frequency conditions (Zhou et al., 1991; Chang et al., 2020):

$$Q_d = (1+\phi) Q_f D_u \tag{4a}$$

where Q_f is the peak flood discharge of clean water (m^3/s); Q_d is the peak flow of the debris flow (m^3/s); D_u is the blockage amplification factor; ϕ is the solids concentration, $\phi = (\gamma_d - 1)/(\gamma_s - \gamma_d)$; and γ_d and γ_s are the densities of the debris flow and solid materials (t/m^3), respectively.

$$Q_f = 0.278 \varphi \frac{S}{\tau^n} F \tag{4b}$$

where φ is the peak runoff coefficient; S is the storm force (mm/h), namely, the maximum 1-h rainstorm intensity; τ is the confluence time (h); n is the rainstorm attenuation index; and F is the watershed area (km^2). The parameters in Eq. (4b) can be obtained by consulting the calculation manual and can be calculated as follows (Sichuan Hydrological Manual 1984; Cui et al., 2023):

$$\varphi = 1 - 1.1 \frac{\mu}{S} t_0{}^n \tag{5a}$$

https://doi.org/10.5194/egusphere-2025-772
Preprint. Discussion started: 11 June 2025

$$S = H_1 K_1 \tag{5b}$$

$$t = t_0 \varphi^{-\frac{1}{4-n}} \tag{5c}$$

$$n = 1 + 1.285\left(\lg \frac{H_1 K_1}{H_6 K_6}\right) \tag{5d}$$

$$\mu = 3.6 K_p F^{-0.19} \tag{5e}$$

$$t_0 = \left(\frac{0.383}{m S^{1/4} / \theta}\right)^{\frac{4}{4-n}} \tag{5f}$$

$$m = 0.221 \theta^{0.204} \tag{5g}$$

$$\theta = \frac{L}{J^{1/3} F^{1/4}} \tag{5h}$$

where μ is the current generation parameter (mm/h); t_0 is the confluence time of the basin; H_1 and H_6 are the 1- and 6-h average rainfall amounts, respectively (mm); K_1 and K_6 are the modulus coefficients corresponding to periods H_1 and H_6, respectively; K_p is the modulus ratio coefficient of the Pearson curve; m is the confluence parameter; θ is the watershed coefficient; J is the slope of the channel; and L is the main channel length (km).

Finally, we combined the results of the two peak discharge calculation methods to determine the peak discharges of the postfire debris flows in the G1 and G2 gullies at different frequencies (Fig. 6).

https://doi.org/10.5194/egusphere-2025-772
Preprint. Discussion started: 11 June 2025

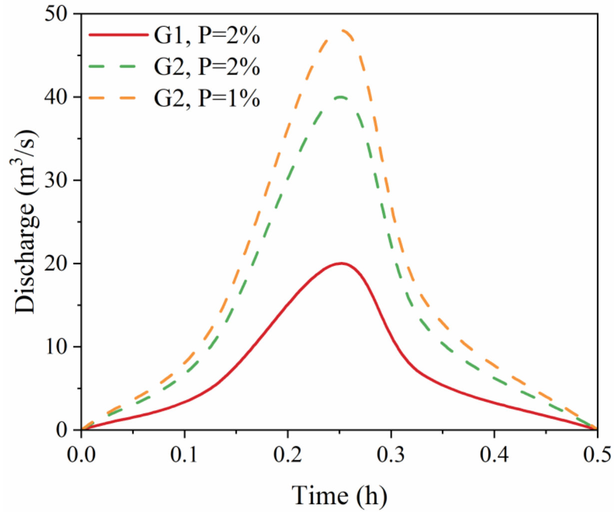

Figure 6 Flow hydrographs of the G1 and G2 gullies at different frequencies.

3.3 FLO-2D numerical simulation of disaster scenarios

3.3.1 Governing equations for rainfall runoff and debris flows

The two-dimensional numerical debris flow evolution model FLO-2D was applied to simulate the runout process and to quantify key metrics of debris flows in the G1 and G2 gullies (Wang et al., 2024; Si et al., 2022; Zhang et al., 2018; Chang et al., 2020). On the basis of 2D shallow water equations, mass and momentum conservation equations are employed in the FLO-2D model as the governing equations:

$$i = \frac{\partial h}{\partial t} + \frac{\partial h \partial V_x}{\partial x} + \frac{\partial h \partial V_y}{\partial y} \tag{6a}$$

$$S_{fx} = S_{ox} - \frac{\partial h}{\partial x} - \frac{V_x}{g}\frac{\partial V_x}{\partial x} - \frac{V_y}{g}\frac{\partial V_x}{\partial y} - \frac{1}{g}\frac{\partial V_x}{\partial t} \tag{6b}$$

$$S_{fy} = S_{oy} - \frac{\partial h}{\partial y} - \frac{V_y}{g}\frac{\partial V_y}{\partial y} - \frac{V_x}{g}\frac{\partial V_y}{\partial x} - \frac{1}{g}\frac{\partial V_y}{\partial t} \tag{6c}$$

where h is the flow depth; V_x and V_y are the depth-averaged velocities along the horizontal

https://doi.org/10.5194/egusphere-2025-772
Preprint. Discussion started: 11 June 2025

x and y coordinates, respectively; i is the intensity at the flow surface; and S_{fx} and S_{fy} are the friction slopes, expressed as functions of bed slopes S_{ox} and S_{oy}, respectively, the pressure gradient and the convective and local acceleration terms (Chen et al., 2021). The total friction slope, S_f, is the sum of the yield slope, the viscous slope, and the turbulent dispersive slope (Zhang et al., 2018), which can be obtained as follows:

$$S_f = \frac{\tau_y}{\gamma_m h} + \frac{K\eta v}{8\gamma_m h^2} + \frac{n_{td}^2 v^2}{h^{4/3}} \tag{7}$$

where η is the dynamic viscosity (Pa·s), and τ_y is the yield stress (Pa), which can be calculated as follows:

$$\eta = \alpha_1 e^{\beta_1 C_v} \tag{8a}$$

$$\tau_y = \alpha_2 e^{\beta_2 C_v} \tag{8b}$$

where C_v is the sediment concentration, and α_1, α_2, β_1, and β_2 are empirical coefficients.

The FLO-2D simulations were conducted by adding elevation data of the computation area to the grid, which was set to 5 m×5 m, after which the inlet and outlet conditions, the rheological parameters (Table 2), the duration of the debris inflow hydrograph (i.e., 30 min) and the peak discharge were defined. Finally, the dynamics and key parameters, such as the flow depth and flow velocity, were obtained.

Table 2. the rheological parameters for the debris flow simulation.

Parameters		Value
Manning's roughness coefficient (n)		0.10
Flow resistance parameter (K)		2,280
Sediment concentration (C_v)		0.49
Viscosity coefficients	α_1	0.81

https://doi.org/10.5194/egusphere-2025-772
Preprint. Discussion started: 11 June 2025

	β_1	13.72
Yield stress coefficients	α_2,	0.00462
	β_2	11.24

3.3.2 Model calibration and validation

To ensure accuracy, the methodology proposed by Scheidl and Rickenmann (2010) was adopted to validate the simulation results (Table 3). We measured the observed depositional fan area through field investigations and the predicted depositional fan area obtained with the FLO-2D model (Chen et al., 2021). The subareas (X, Y and Z) were obtained via the overlay of the predicted deposition area with the observed deposition area. We assessed the overall reconstruction accuracy via the following evaluation parameters (Chen et al., 2021; Wang et al., 2024):

$$\varepsilon = \frac{S_X}{S_{observed}} - \frac{S_Y}{S_{observed}} - \frac{S_Z}{S_{observed}} + \frac{V_X}{V_{observed}} \tag{9}$$

$$\delta = \frac{\varepsilon + 2}{4} \tag{10}$$

where S_X, S_Y, and S_Z are the positive accuracy region, negative accuracy region, and missing accuracy region, respectively; S_{observed} is the actual impact zone; V_X is the correct judgement volume; V_{observed} is the actual volume; and δ is the normalized accuracy value, with values ranging from 0 to 1.

Table 3 Calibration parameters and accuracy of the numerical simulation results

Parameters	Sx (10^3 m^2)	Sy (10^3 m^2)	Sz (10^3 m^2)	S_{observed} (10^3 m^2)	Vx (10^4 m^3)	V_{observed} (10^4 m^3)	ε	δ
Impact zone	13.59	1.83	1.06	15.42	0.73	0.81	1.59	0.90

https://doi.org/10.5194/egusphere-2025-772
Preprint. Discussion started: 11 June 2025

3.4 Development of empirical vulnerability models for buildings

3.4.1 Damage class of buildings

Kule village encompasses a total of 128 buildings, with 36 buildings on the left bank affected by postfire debris flows in the G1 gully. The damage to buildings notably depends on their structural type, material resistance and distribution density (Zhang et al., 2018). In the study area, 95% of the affected main building structures are BC structural-type buildings, which are widely distributed in mountainous areas across China (Chen et al., 2021). We subsequently aimed to develop vulnerability curves for BC buildings. Most buildings in the study area comprise 1–3 floors, and the building height ranges from 3–8 m. To determine the degree of damage to buildings caused by debris flows, it is necessary to establish a classification standard on the basis of the actual structural and damage degree conditions (Hu et al., 2012; Lee et al., 2024). Table 4 provides the four categories of damage to a given structure and the corresponding vulnerability index values, including slight, moderate, extensive, and complete damage. On the basis of the above assumptions and analysis, damaged buildings affected by debris flows in Kule village were constructed (Appendix A).

Table 4 Damage classes and definitions for buildings (Hu et al., 2012; Wang et al., 2024; Lee et al., 2024)

Damage class	Damage description	Value
Slight	Minor nonstructural damage occurred, with no impact on stability; damage was limited to furnishings and fittings.	0.1~0.3
Moderate	Cracks appeared in the wall, but stability remained unaffected; repairs are not urgent.	0.3~0.6

https://doi.org/10.5194/egusphere-2025-772
Preprint. Discussion started: 11 June 2025

Extensive	The structure is partly destroyed, with partial loss of external and internal walls; evacuation is necessary; and reconstruction of damaged parts is required.	0.6~0.8
Complete	The structure is completely destroyed; evacuation is imperative; and complete reconstruction is necessary.	0.8~1.0

3.4.2 Debris flow intensity

In this study, six commonly used debris flow intensities were selected as multidimensional indicators of the destruction potential (Quan Luna et al., 2011; Eidsvig et al., 2014; Kang and Kim, 2016; Zhang et al., 2018; Chen et al., 2021; Wang et al., 2024; Lee et al., 2024), including the flow depth (*h*), flow velocity (*v*), impact pressure (*p*), momentum flux (*f*), overturning moment (*m*), and relative burial height (*b*).

The flow impact pressure includes both hydrostatic and hydrodynamic forces (Kang and Kim, 2016; Wang et al., 2024), and the total impact pressure exerted by a debris flow can be expressed as:

$$p = \frac{1}{2}\rho g h + \rho v^2 \tag{11}$$

where p is the impact pressure (Pa); v is the flow velocity (m/s); and h is the flow depth (m).

The momentum flux can be obtained by multiplying the flow depth and the square of the flow velocity (Jakob et al., 2012; Chen et al., 2021):

$$f = hv^2 \tag{12}$$

where f is the momentum flux (m^3/s^2).

The overturning moment of a debris flow is related to the maximum flow velocity and

https://doi.org/10.5194/egusphere-2025-772
Preprint. Discussion started: 11 June 2025

depth at which it collides with a given structure, as reported by Zhang et al. (2018):

$$m = vh \tag{13}$$

where m is the overturning moment (m^2/s).

The relative burial height is defined by the deposition height and the affected building height to represent the degree of burial damage (Totschnig et al., 2011; Zhang et al., 2018):

$$b = \frac{h_d}{h_b} \tag{14}$$

where b is the relative burial height, h_d is the deposition height (m), and h_b is the building height (m).

3.4.3 Vulnerability curve

The vulnerability model captures the relationship between the probability of building damage reaching a certain state and the debris flow intensity (Cui et al., 2011). Notably, postdisaster data-driven vulnerability curves can be expressed via function models (Fuchs et al., 2019). Currently, many vulnerability functions, such as logistic, Weibull, exponential, power law and Avrami functions, are employed (Quan Luna et al., 2011; Eidsvig et al., 2014; Chen et al., 2021; Lee et al., 2024). However, the uncertainties in these models originate from the curve fitting process. For example, the use of the exponential function cannot guarantee that the curve passes through the origin. Therefore, recent studies have indicated that LNCDF-based vulnerability curves provide better performance (Luo et al., 2023):

$$V = \Phi\left[\frac{1}{\beta}\ln\left(\frac{I}{I_{\mathrm{m}}}\right)\right] \tag{15}$$

where β is the standard deviation of the logarithm of the hazard intensity; I is the debris flow hazard intensity; I_{m} is the median hazard intensity; and Φ is the LNCDF, which can be

https://doi.org/10.5194/egusphere-2025-772
Preprint. Discussion started: 11 June 2025

expressed as follows:

$$\Phi(x)=\int_0^x \frac{1}{\sqrt{2\pi}\sigma t} e^{-\frac{(\ln(t)-\mu)^2}{2\sigma^2}} dt \tag{16}$$

where μ is the mean of the LNCDF, and σ is the standard deviation of the LNCDF.

4. Results

4.1 Reproduction of the debris flow intensity and building damage in the G1 gully

Figure 7 shows the characteristics of the degree of damage to buildings and the distribution of buildings in the G1 gully. There are 36 buildings on the left bank of Kule village affected by postfire debris flows in the G1 gully. Notably, the numbers of buildings with slight, moderate, extensive and complete damage are 8, 7, 9 and 12, respectively. Figure 8 shows that the FLO-2D simulations reproduce the runout process of debris flows in the G1 gully that occurred on 10 May 2024, and distribution maps of the inundation area, flow velocity and flow depth were obtained. The buildings were impacted and buried by debris flows, the flow depth near the impacted buildings ranged from 0.25 to 2.61 m, and the flow velocity near the buildings ranged from 0.04 to 1.93 m/s. This occurred because the debris flow energy partly dissipates under the influence of building groups, and sediment is deposited inside the buildings. The debris flow also partially entered the main river, causing blockages at bridges connecting the villages on both sides (Fig. 8).

https://doi.org/10.5194/egusphere-2025-772
Preprint. Discussion started: 11 June 2025

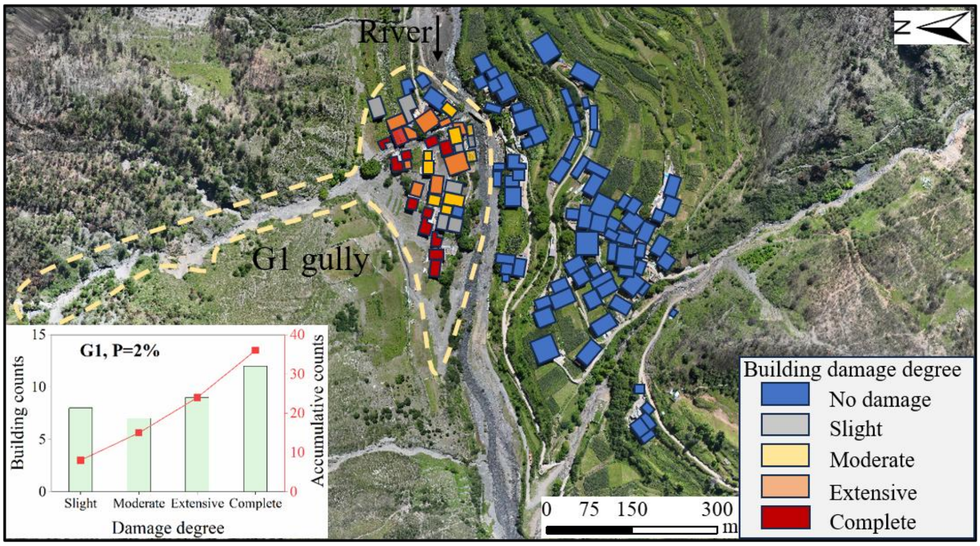

Figure 7 The counts of building damage degree and spatial distribution of buildings.

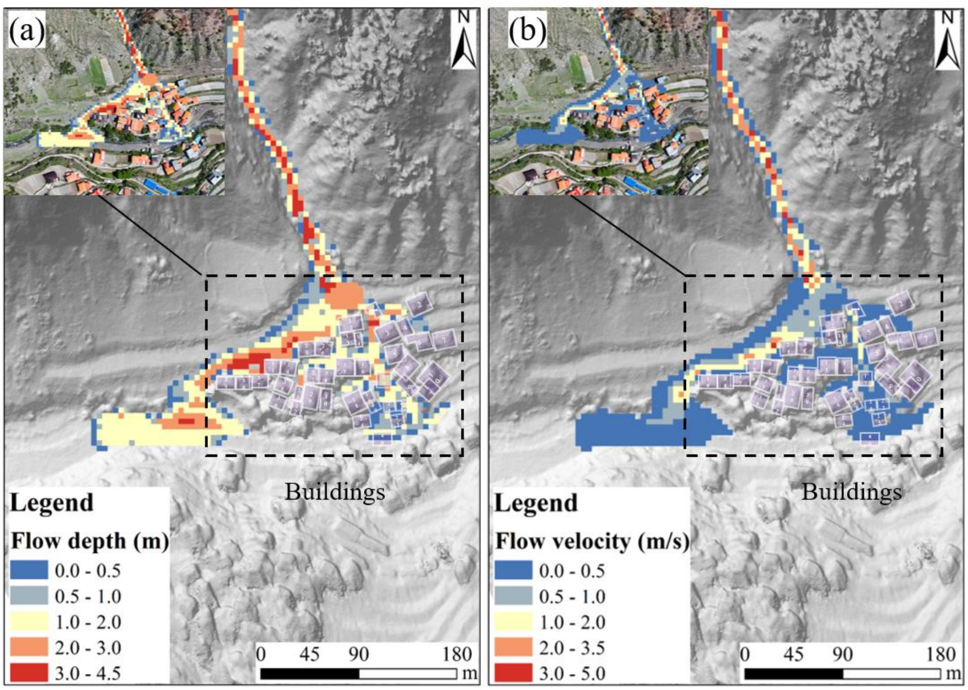

Figure 8 Reconstruction of the debris flow in the G1 gully using the FLO-2D model: (a) Flow depth map; (b) flow velocity map.

https://doi.org/10.5194/egusphere-2025-772
Preprint. Discussion started: 11 June 2025

4.2 Construction of the vulnerability model

Figure 9 shows six groups of developed vulnerability curves for the 2024 postfire debris flow events in the G1 gully, including the flow depth, flow velocity, impact pressure, momentum flux, overturning moment and relative burial height. The vulnerability curve can be obtained via a continuum function relating the debris flow intensity (X-axis) to the degree of building damage (Y-axis). The LNCDF effectively described the trend in the data. Each vulnerability curve is a monotonically increasing function, indicating that with increasing debris flow intensity, the probability of failure gradually increases. When the slope of the vulnerability curve suddenly increases, the ability of the structure to resist disasters rapidly decreases after critical-strength debris flow disaster occurrence, leading to a rapid increase in the probability of failure. Specifically, to reach a maximum vulnerability value of 1, BC buildings necessitate a flow depth greater than 6 m, a flow velocity of 5 m/s, an impact pressure of 50 kPa, a momentum flux of 50 kPa, and an overturning moment of 40 m^2/s. However, completely damaged buildings (with a vulnerability value exceeding 0.8) can no longer function properly. Thus, the critical value of failure is lower, corresponding to a flow depth of 2.5 m, a flow velocity of 1.3 m/s, an impact pressure of 25 kPa and a relative burial height of 0.48. Additionally, the responses of the various indicators to vulnerability differed, and these differences are analysed in greater detail in the subsequent chapter.

https://doi.org/10.5194/egusphere-2025-772
Preprint. Discussion started: 11 June 2025

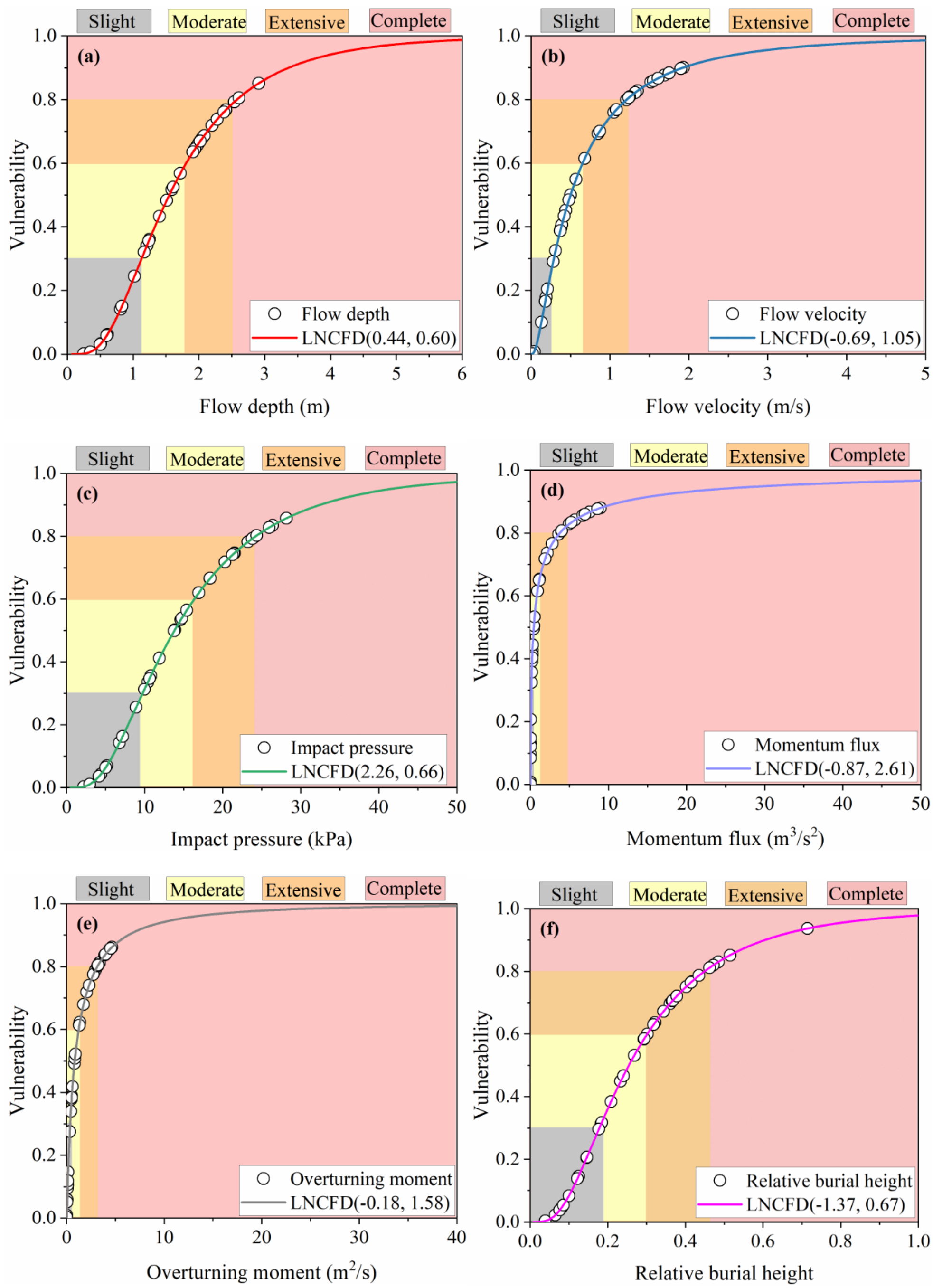

Figure 9 Vulnerability curves for debris flow intensities: (a) Flow depth, (b) flow velocity, (c) impact pressure, (d) momentum flux, (e) overturning moment, and (f) relative burial height.

https://doi.org/10.5194/egusphere-2025-772
Preprint. Discussion started: 11 June 2025

4.3 Prediction of the debris flow intensity and application of the damaged building vulnerability model in the G2 gully

Potential postfire debris flow events may occur in the G2 gully, thus posing a serious threat to buildings on the right bank of Kule village. Figure 10 shows the prediction of potential debris flows in the G2 gully using the FLO-2D model under reproduction frequency conditions of P=2% (the peak flow is 40 m^3/s) and P=1% (the peak flow is 48 m^3/s). The simulated scenarios revealed that the buildings near the channel were significantly affected by the debris flow, and the debris flow flowed into the main river, causing deposition and blockage. The maximum flow depth and flow velocity around the buildings are 3.50 m and 2.36 m/s, respectively. A comparison of the flow depths between the two recurrence periods revealed that the maximum value under P=1% surpassed that under P=2 by 20%.

Then, by applying the established vulnerability model to the debris flow intensity data of the G2 gully (Fig. 11), the vulnerability value of damaged buildings in the G2 gully can be calculated from the generated curves (Appendix B). Next, four categories were determined through a combination of vulnerability values and the damage classification system. Figure 12 shows the predicted building damage degree and the spatial distribution under different recurrence periods. The predicted total number of affected buildings is 24, and the numbers of buildings with slight, moderate, extensive and complete damage are 4, 12, 4 and 4, respectively, for P=2%. Concurrently, the numbers of buildings with extensive and complete damage exhibit a corresponding uptick under longer recurrence periods (Fig. 12).

https://doi.org/10.5194/egusphere-2025-772
Preprint. Discussion started: 11 June 2025

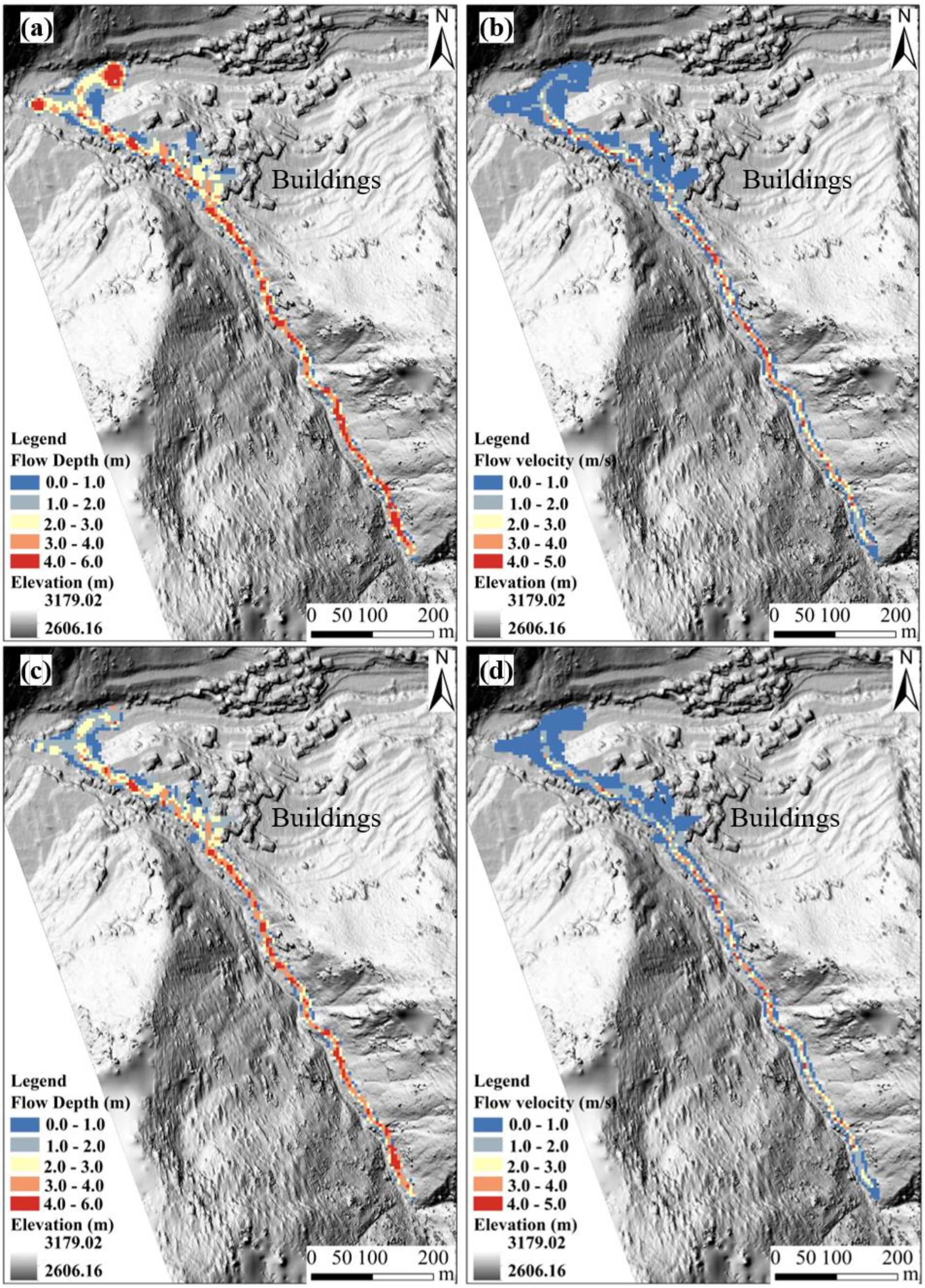

Figure 10 Prediction of the potential debris flow in the G2 gully using the FLO-2D model: (a) Flow depth, P=2%; (b) flow velocity, P=2%; (c) flow depth, P=1%; (d) flow velocity, P=2%.

https://doi.org/10.5194/egusphere-2025-772
Preprint. Discussion started: 11 June 2025

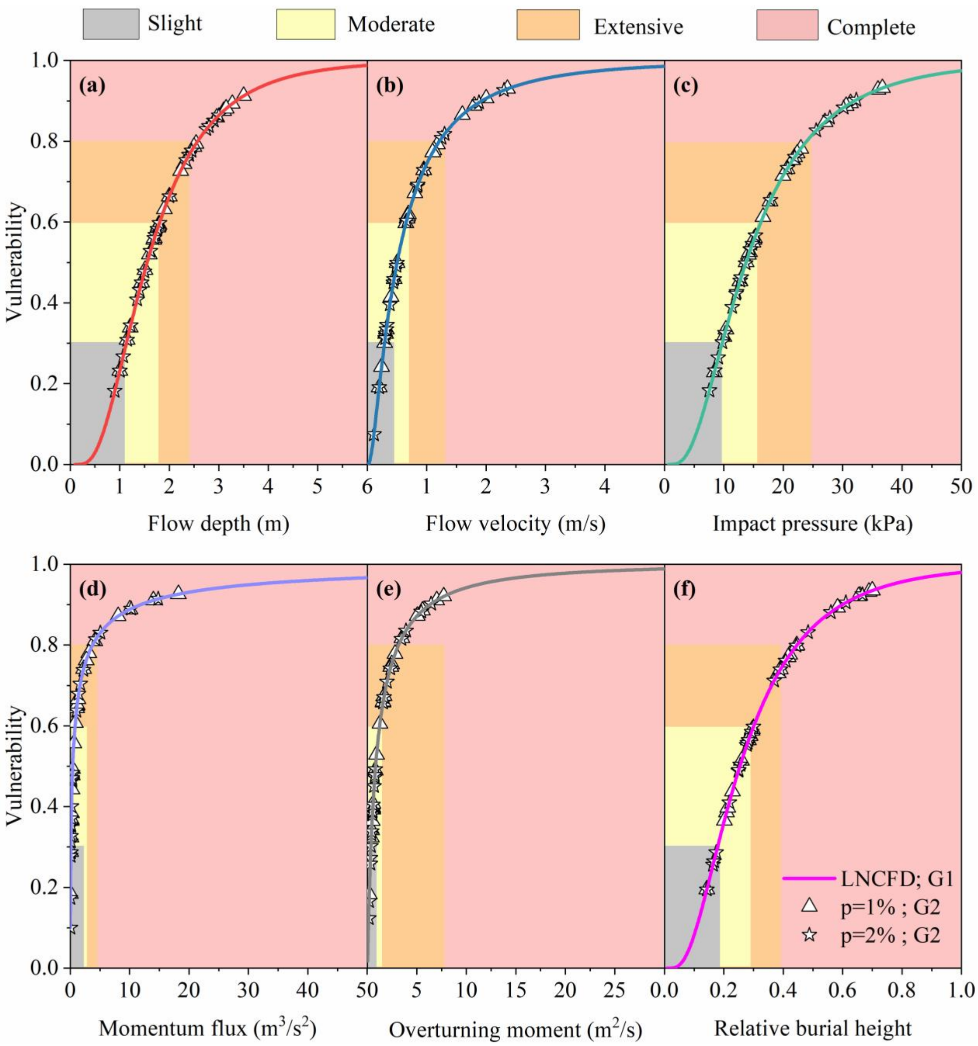

Figure 11 Vulnerability curves for different intensities of debris flows in the G2 gully according to the established vulnerability model for determining the building damage status: (a) Flow depth, (b) flow velocity, (c) impact pressure, (d) momentum flux, (e) overturning moment, and (f) relative burial height.

https://doi.org/10.5194/egusphere-2025-772
Preprint. Discussion started: 11 June 2025

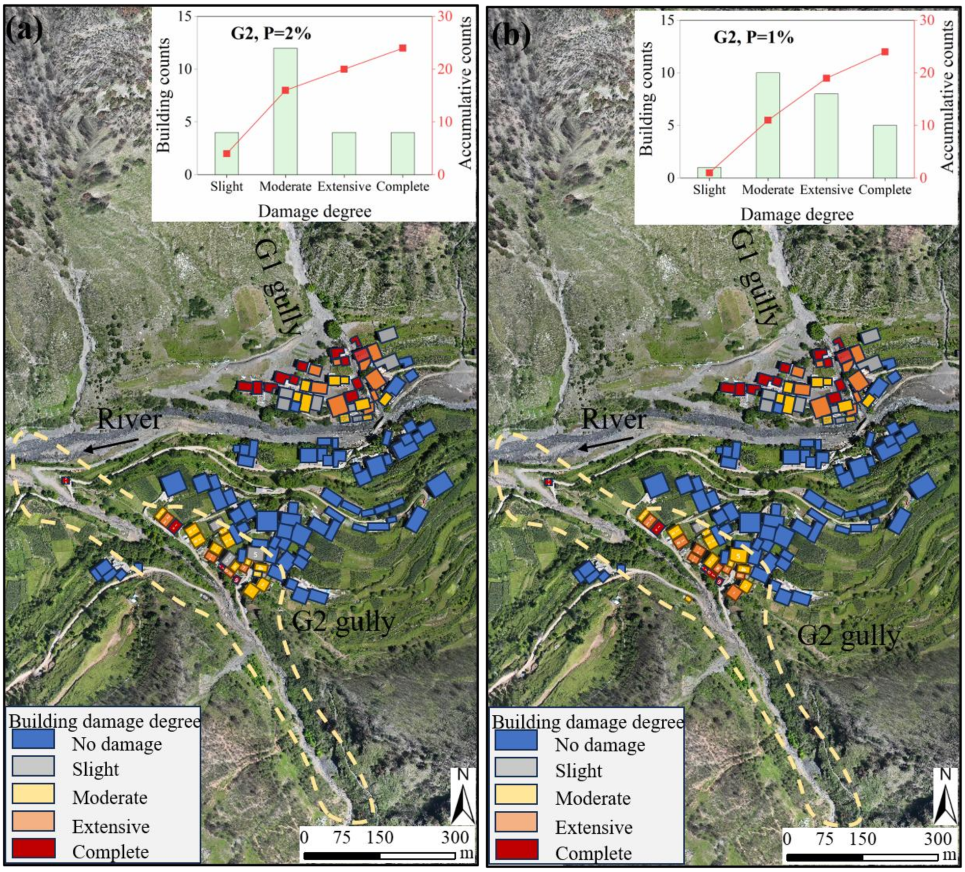

Figure 12 Predicted building counts with degree of damage and the spatial distribution in the G2 gully under different recurrence periods: (a) P=1%; (b) P=2%.

5. Discussion

5.1 Comparison of building vulnerability models

5.1.1 Comparison of debris flow intensity indicators

As mentioned earlier, we selected six indicators of the debris flow intensity to construct a building vulnerability model, but the vulnerability values also varied among the different indicators. Figure 13 shows the statistics of the total number of buildings and the vulnerability value under six debris flow intensities and four damage degrees in the G1 and G2 gullies of Kule village. The line width indicates the number of damaged buildings and their vulnerability value, with a thicker line indicating a higher value. The buildings in Kule village mainly exhibited moderate and complete damage. Under the same damage state, the maximum difference in vulnerability between the different strength indicators was 0.20, and differences in the predicted vulnerability can easily lead to inaccurate category determination (Luo et al., 2023). Therefore, we must conduct a more detailed comparative analysis of the different debris flow intensity indicators.

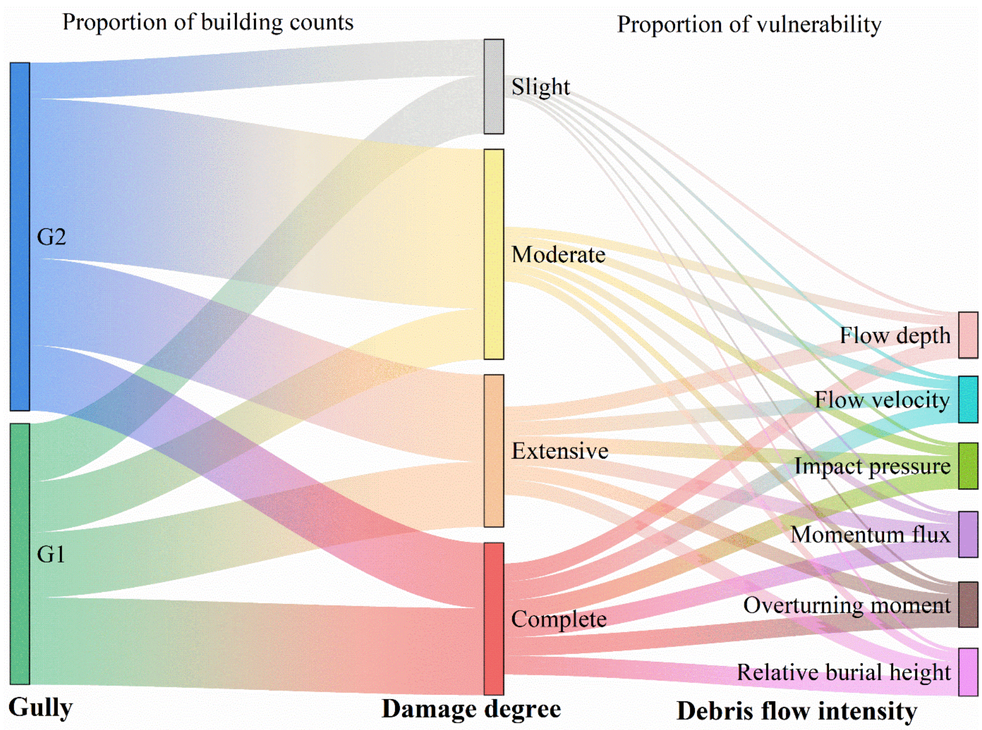

Figure 13 Statistics on the number of buildings and vulnerability under different debris flow intensities and damage degrees in the G1 and G2 gullies of Kule village.

https://doi.org/10.5194/egusphere-2025-772
Preprint. Discussion started: 11 June 2025

We first normalized the debris flow intensity and vulnerability values, which can be calculated as follows (Zhang et al., 2024):

$$I^* = \frac{I - \min(I)}{\max(I) - \min(I)} \tag{17a}$$

$$V^* = \frac{V - \min(V)}{\max(V) - \min(V)} \tag{17b}$$

where I^* and V^* are the normalized values of the debris flow intensity and vulnerability, respectively.

Then, we compared the differences and sensitivities of the six curves in evaluating the vulnerability of damaged buildings (Fig. 14). In terms of the properties of the normalized LNCDF curves, the larger the mean (μ) value is, the more the curve shifts to the right, indicating an increased probability of I^* attaining a larger value. The higher the standard deviation (σ) is, the flatter the curve and the more dispersed the probability distribution. Conversely, the lower σ, the steeper the curve is, indicating a narrower range of I^* values and a more concentrated probability distribution. As shown in Fig. 14, the momentum flux and overturning moment curves are steeper, indicating higher sensitivity of these indicators accompanied by a rapid increase in the probability of failure and more effective determination of the boundaries of the different damage categories (Barnhart et al., 2024). Additionally, the flow depth and impact pressure curves are relatively gradual, with low sensitivity, but the stability and accuracy of determining the degree of damage are greater (Wang et al., 2024; Lee et al., 2024). Furthermore, the impact pressure provides a more intuitive physical interpretation, indicating the destructiveness of debris flows in relation to both the hydrostatic pressure and dynamic

https://doi.org/10.5194/egusphere-2025-772
Preprint. Discussion started: 11 June 2025

overpressure, which has facilitated its widespread adoption in disaster risk assessment (Quan Luna et al. 2011; Wang et al., 2024).

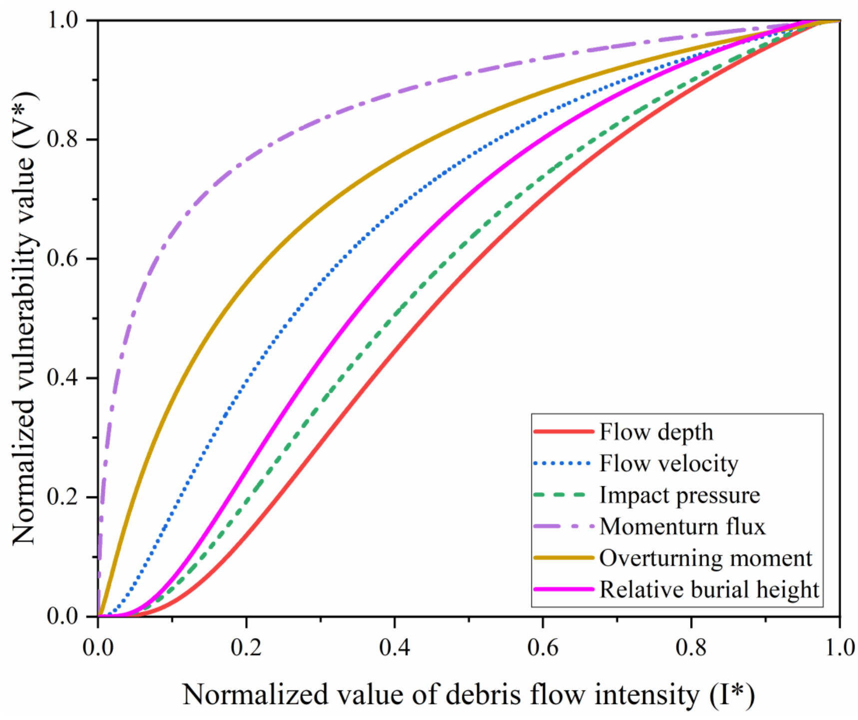

Figure 14 Comparison of vulnerability curves of the normalized debris flow intensity.

5.1.2 Comparison of the proposed vulnerability models for brick–concrete buildings

Table 5 shows a comparison between the proposed vulnerability models for BC buildings and models established in previous studies (Quan Luna et al. 2011; Eidsvig et al. 2014; Kang and Kim, 2016; Zhang et al., 2018; Chen et al., 2021; Wang et al., 2024; Lee et al., 2024). Specifically, Quan Luna et al. (2011) proposed two vulnerability curves for 13 unreinforced buildings in Valtellina Valley, Northern Italy. Eidsvig et al. (2014) established vulnerability curves for 53 buildings affected by debris flows in Martell Valley, South Tyrol, Italy. Kang and Kim (2016) proposed three vulnerability curves using data from 16 damaged buildings and 11

https://doi.org/10.5194/egusphere-2025-772
Preprint. Discussion started: 11 June 2025

debris flows that occurred in Korea. Zhang et al. (2018) developed six vulnerability curves to assess damage to BC buildings caused by debris flows in Zhouqu County, northwestern China. Chen et al. (2021) constructed a physical fragility curve for 19 BC buildings damaged by debris flows that occurred in the Cutou Gully, Wenchuan County, China. Wang et al. (2024) developed two vulnerability curves for 41 damaged buildings in the Wangzhuangwu watershed, Zhejiang Province, eastern China. Lee et al. (2024) proposed a vulnerability curve for 39 buildings and conducted a back analysis of 22 debris flow events that occurred in South Korea.

Figure 15 shows a comparison of the various vulnerability curves for different debris flow intensities. First, the flow depth vulnerability curve developed in this study is close to those of Quan Luna et al. (2011) and Zhang et al. (2018) and falls between those established by Wang et al. (2024) and Kang and Kim (2016), which suggests the existence of different threshold values (Fig. 15a). The complete damage threshold (V=0.8) is reached at 2.5 m, whereas the value is 1.3 m in Wang et al. (2024) and 4.5 m in Kang and Kim (2016). These variations may be attributed to regional and national differences, including differences in building codes and construction techniques (Wang et al., 2024). Second, the slope of the flow velocity vulnerability curve established in this study is higher than those of Zhang et al. (2018) and Kang and Kim (2016), which may be due to differences in flow properties such as the debris flow volume and density (Fig. 15b). Third, the slope of the proposed impact force vulnerability curve is initially high, which is similar to the findings of Zhang et al. (2018). The slope subsequently decreases within the complete damage class, and the pressure reaches 60 kPa (V=1.0), which is similar to the results of Kang and Kim (2016) but greater than the values of 25 kPa reported by Wang et

https://doi.org/10.5194/egusphere-2025-772
Preprint. Discussion started: 11 June 2025

al. (2024), 38 kPa reported by Quan Luna et al. (2011) and 42 kPa reported by Lee et al. (2024). These differences may be due to the conditions of the building shape, position, materials (Kang and Kim 2016; Lee et al., 2024), and number of data points (Zhang et al., 2018), which greatly affect the degree of damage (Fig. 15c). Fourth, the momentum flux vulnerability curve proposed in this study is similar to that of Chen et al. (2011) but far lower than that of Zhang et al. (2018). The vulnerability factor of BC buildings reached 1.0 under a momentum flux of 36 m^3/s^2 in Chen et al. (2021), 90 m^3/s^2 in this study, and 131 m^3/s^2 in Zhang et al. (2018), as shown in Fig. 15d. This may occur because the momentum flux is relatively more sensitive (Fig. 14), and the scale of the Zhouqu debris flow is much larger (Zhang et al., 2018). Fifth, the slope of the overturning moment vulnerability curve developed in this study is steeper than that of Zhang et al. (2018), which reaches the complete damage threshold (V=0.8) at 4.0 m^2/s, compared with the value of 20.1 m^2/s obtained by Zhang et al. (2018), as shown in Fig. 15e. This finding may be related to the differences in debris flow characteristics and building damage classification standards (Quan Luna et al., 2011). Finally, among the different relative burial height vulnerability curves, the slope of the proposed vulnerability curve is much higher than that of Zhang et al. (2018), with slight building damage (V<0.3) starting to decline later (Fig. 15f). When complete building damage occurs (V=0.8), the relative burial height reaches 0.42 for the curve established in this study and 0.3 for the curve of Zhang et al. (2018). In contrast, our vulnerability estimation is more conservative and requires a greater debris flow intensity to cause complete damage, which may be attributed to differences in the number of floors, and the height of hipped roofs may be included in the total building height in different regions

https://doi.org/10.5194/egusphere-2025-772
Preprint. Discussion started: 11 June 2025

(Totschnig et al., 2011; Zhang et al., 2018). Thus, we may require more detailed classification of damaged buildings in the debris flow event database (Kang and Kim 2016).

Table 5 Comparison of the vulnerability curves of brick–concrete buildings for different debris flow intensities between this study and previous studies

Researchers	Debris flow density	Vulnerability functions	Vulnerability model for BC buildings
Quan Luna et al. (2011)	Flow depth, h Impact pressure, p	Logistic	$V=\frac{1.49\times(h/2.51)^{1.938}}{1+(h/2.51)^{1.938}}$ $V=\frac{1.59\times(p/28.16)^{1.808}}{1+(p/28.16)^{1.808}}$
Eidsvig et al. (2014)	Flow depth, h	Weibull distribution	$V=1-e^{-0.27h^{2.97}}$
Kang and Kim (2016)	Flow depth, h Flow velocity, v Impact pressure, p	Sigmoid, S-shaped	$V=1-e^{-0.170h^{1.537}}$ $V=1-e^{-0.009v^{2.775}}$ $V=1-e^{-0.005p^{1.690}}$
Zhang et al. (2018)	Flow depth, h Flow velocity, v Impact pressure, p Momentum flux, f Overturning moment, m Relative burial height, b	Logistic	$V=\frac{0.12\times h^{3.39}}{1+9.24h^{3.39}}$ $V=\frac{0.17\times v^{2.45}}{1+6.54\times v^{2.45}}$ $V=\frac{0.08\times p^{1.08}}{1+15.45p^{1.08}}$ $V=\frac{0.24\times f^{0.40}}{1+10.23\times f^{0.40}}$ $V=\frac{0.15\times m^{1.15}}{1+7.83m^{1.15}}$ $V=\frac{1096\times b^{1.54}}{1+0.0009b^{1.54}}$
Chen et al. (2021)	Momentum flux, f	Exponential	$V=1/(1+e^{-1.036f+4.721})$
Wang et al. (2024)	Flow depth, h Impact pressure, p	Weibull distribution	$V=1-e^{-0.53h^{3.26}}$ $V=1-e^{-0.49(0.1p)^{2.65}}$
Lee et al. (2024)	Impact pressure, p	Avrami	$V=1.129(1-e^{-0.007\times p^{1.530}})$
This study	Flow depth, h Flow velocity, v Impact pressure, p Momentum flux, f Overturning moment, m Relative burial height, b	Lognormal cumulative distribution function	$V=\Phi\left[\frac{1}{0.60}\ln\left(\frac{h}{e^{0.44}}\right)\right]$ $V=\Phi\left[\frac{1}{1.05}\ln\left(\frac{v}{e^{-0.69}}\right)\right]$ $V=\Phi\left[\frac{1}{0.66}\ln\left(\frac{p}{e^{2.26}}\right)\right]$ $V=\Phi\left[\frac{1}{2.61}\ln\left(\frac{f}{e^{-0.87}}\right)\right]$ $V=\Phi\left[\frac{1}{1.58}\ln\left(\frac{m}{e^{-0.18}}\right)\right]$ $V=\Phi\left[\frac{1}{0.67}\ln\left(\frac{b}{e^{-1.37}}\right)\right]$

https://doi.org/10.5194/egusphere-2025-772
Preprint. Discussion started: 11 June 2025

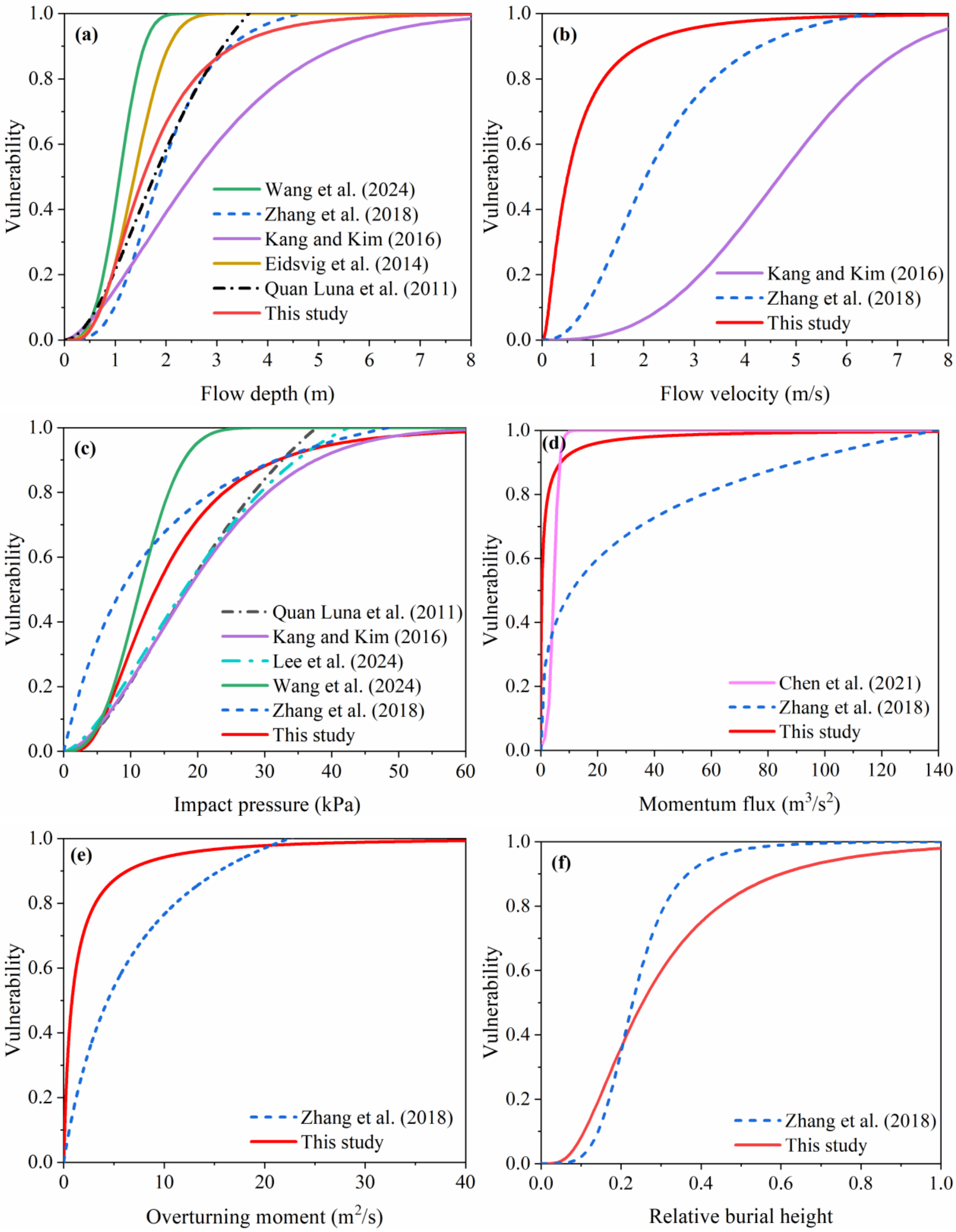

Figure 15 Comparison of the vulnerability curves with previous models for different debris flow intensities.

5.1.3 Comparison of vulnerability functions

https://doi.org/10.5194/egusphere-2025-772
Preprint. Discussion started: 11 June 2025

The differences between the various vulnerability curves also depend on the vulnerability function models employed. Table 6 provides the existing vulnerability function models, including logical functions, Weibull functions, exponential functions, LNCDF models and Avrami functions (Quan Luna et al., 2011; Eidsvig et al., 2014; Kang and Kim, 2016; Zhang et al., 2018; Chen et al., 2021; Luo et al., 2023; Wang et al., 2024; Lee et al., 2024).

We analysed the performance of the function models using data from this study and previous research (Fig. 16). The performance of different models was comparatively analysed via four dimensionless performance indices (Table 6), namely, the coefficient of determination (R^2), the mean relative error (MRE), the Theil inequality coefficient (TIC), and the prediction accuracy factor (PAF). Notably, lower MRE and TIC values reflect higher model performance. Additionally, the closer the PAF value is to 1, the better the agreement between the calculated and experimental values (the higher the prediction accuracy). These indices can be calculated as follows (Lee et al., 2024; Wang et al., 2018):

$$R^2 = 1 - \frac{\sum_{i=1}^{N}\left(I_{cal,i} - I_{obs,i}\right)^2}{\sum_{i=1}^{N}\left(I_{cal,i} - \bar{I}_{obs,i}\right)^2} \tag{18}$$

$$MRE = \frac{1}{N}\sum_{i=1}^{N}\frac{\left|I_{cal,i} - I_{obs,i}\right|}{I_{obs,i}} \tag{19}$$

$$TIC = \frac{\sqrt{\left(\sum_{i=1}^{N}\left(I_{cal,i} - I_{obs,i}\right)^2\right)/N}}{\sqrt{\left(\sum_{i=1}^{N} I^2_{cal,i}\right)/N} + \sqrt{\left(\sum_{i=1}^{N} I^2_{obs,i}\right)/N}} \tag{20}$$

$$PAF = 10^{\frac{\sum_{i=1}^{N}\log\left|I_{cal,i}/I_{obs,i}\right|}{N}} \tag{21}$$

where N is the total number of data points, and $I_{cal,i}$ and $I_{obs,i}$ are the calculated and observed

https://doi.org/10.5194/egusphere-2025-772
Preprint. Discussion started: 11 June 2025

values of case i, respectively.

The performance values of different function models were compared using the flow depth and impact pressure as examples (Fig. 16). The S-shaped function models (logical, Weibull, Avrami and LNCDF models) clearly performed better than the exponential function model did, whose vulnerability curve did not pass through the origin (Fig. 16a; b) and may be heavily affected by outliers. In addition, the coefficients of determination of all the function models did not significantly differ, with R^2 values exceeding 0.88 (Table 7). This finding indicates that the coefficient of determination only focuses on the degree of fit of the regression equation (Lee et al., 2023), but it is not necessarily better for models with relatively large R^2 values, such as exponential functions (R^2=0.98) with relatively large errors. The coefficient of determination is affected by the complexity of the model, and overfitting may occur, which may lead to the model performing well for training data but exhibiting a poor prediction ability with new data. Therefore, the relative error and prediction accuracy of function models should be accounted for (Wang et al., 2018).

In the comparison of the calculated and observed values, both the exponential and Avrami functions clearly exhibited significant errors (Fig. 16c; d). Specifically, the MRE values for the flow depth were 0.76 and 0.45, respectively, whereas the MRE values for the impact pressure were 0.48 and 0.24, respectively (Table 7). However, the LNCDF model demonstrated the highest statistical significance in terms of the relative error and accuracy, with MRE=0.16 and PAF=1.15 for the flow depth and MRE=0.09 and PAF=1.09 for the impact pressure. In multiple regression models, the coefficient of determination emphasizes the interpretability and fitting

https://doi.org/10.5194/egusphere-2025-772
Preprint. Discussion started: 11 June 2025

performance, whereas the error prioritizes the prediction accuracy of the model. Overall, these two metrics provide complementary insights for evaluating the overall performance of the model. Overall, the performance of the various function models exhibited the following order: LNCDF > logistic > Weibull > Avrami > exponential models. LNCDF-based models are insensitive to single data points because of the statistical parameter curve fitting process for developing these models. It has been demonstrated that the LNCDF model can efficiently increase the prediction performance, leading to a substantial reduction in output uncertainty, and this model is recommended for future applications (Luo et al., 2023).

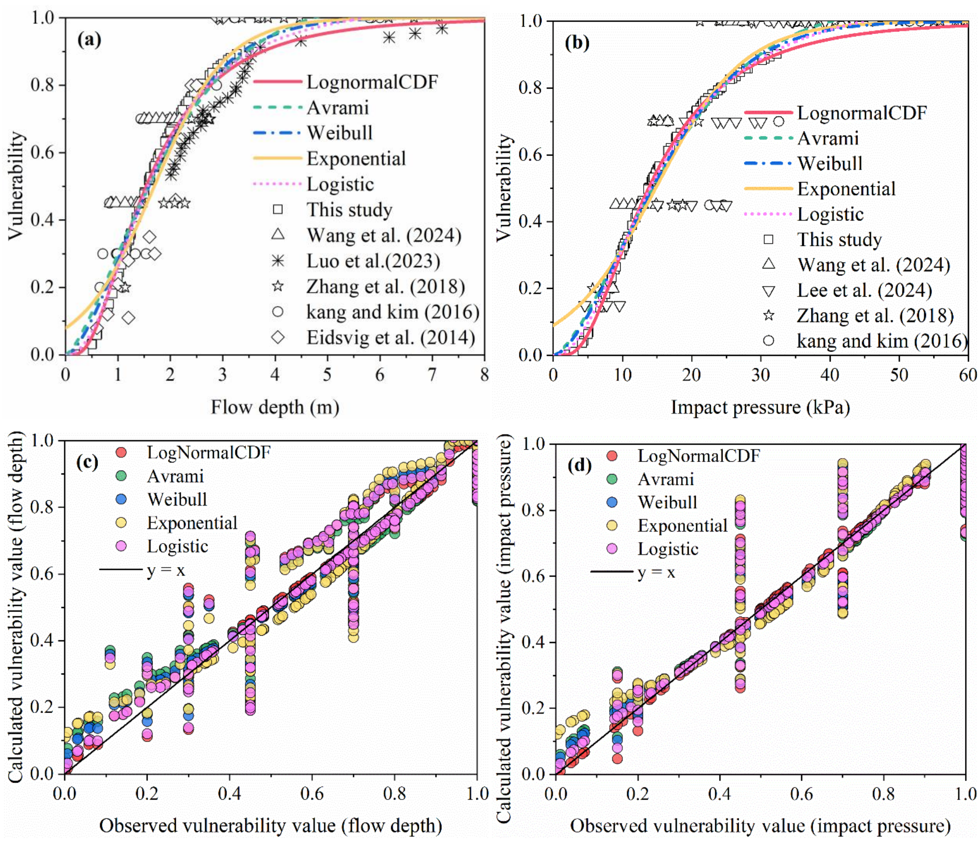

Figure 16 Performance comparison between different vulnerability function models: (a) Flow

https://doi.org/10.5194/egusphere-2025-772
Preprint. Discussion started: 11 June 2025

depth vulnerability models; (b) impact pressure vulnerability models; (c) observation and calculation values of the flow depth; (d) observation and calculation values of the impact pressure.

Table 6 Performance comparison between various data-driven building vulnerability function models

Researchers	Vulnerability models	Function models	Flow depth				Impact pressure			
			R^2	MRE	TIC	PAF	R^2	MRE	TIC	PAF
Quan Luna et al. (2011); Zhang et al. (2018)	Logistic	$V=\frac{a\times(\frac{x}{b})^c}{1+(\frac{x}{b})^c}$	0.98	0.22	0.06	1.17	0.89	0.16	0.06	1.13
Chen et al. (2021)	Exponential	$V=\frac{1}{1+e^{ax+b}}$	0.98	0.76	0.06	1.23	0.88	0.48	0.07	1.19
Eidsvig et al. (2014); Kang and Kim (2016); Wang et al. (2024)	Weibull	$V=1-e^{-(x/a)^b}$	0.88	0.37	0.06	1.20	0.89	0.22	0.06	1.15
Lee et al. (2024)	Avrami	$V=a(1-e^{-bx^c})$	0.99	0.45	0.06	1.21	0.89	0.24	0.06	1.16
Luo et al. (2023); This study	LNCDF	$V=\Phi\left[\frac{1}{\beta}\ln\left(\frac{I}{I_m}\right)\right]$	0.88	0.16	0.06	1.15	0.88	0.09	0.06	1.09

Note: The parameters a, b, and c can be obtained directly by curve fitting.

https://doi.org/10.5194/egusphere-2025-772
Preprint. Discussion started: 11 June 2025

5.1.4 Limitations

Our results provide insights into assessing the vulnerability of buildings to debris flows triggered by wildfires in Yajiang County. A combination of numerical simulation and function model methods provided a distinct advantage in the development of vulnerability curves. The spatial distributions of the flow depth and flow velocity can be visualized, and detailed physical information can be obtained in a specific area (Zhang et al., 2018). Additionally, this study highlights the importance of acknowledging and addressing the inherent uncertainty associated with various debris flow intensity indicators and function models applied in vulnerability assessments via a comparison of existing intensity indicators and evaluating the performance of various function models.

However, there are certain limitations in the research process, which may encompass a wide range of factors. First, during the numerical modelling phase, the changes in terrain and sediment volume caused by the entrainment capacity of debris flows were neglected (Wang et al., 2024), and the sediment concentration along the channel was set to a constant value. With respect to the calibration parameters in the numerical simulation process, we applied a validation model that accounts for the depositional area and runout volume to evaluate the accuracy of the simulation results, thereby neglecting the validation of the flow velocity along the path (Chen et al., 2021). Second, owing to a lack of comprehensive research on the triggering and runoff mechanisms of postfire debris flows (Rengers et al., 2016; Ouyang et al., 2023) and the introduction of burned wood into channels to affect movement (Rengers et al., 2023), only the volume and peak flow of debris flows were considered representative indicators

https://doi.org/10.5194/egusphere-2025-772
Preprint. Discussion started: 11 June 2025

of the recurrence period of debris flow events (Cui et al., 2018; Gorr et al., 2024). The influences of certain geological variables, such as the particle size distribution, viscosity and water content, were not considered (Chen et al., 2021). Third, differences in the vulnerability curves of different indicators could cause uncertainty in vulnerability assessments (Luo et al., 2023), where the percentage of buildings categorized may be inconsistent. The slopes of the LNCDF-based curves increase slowly during the latter half, making it easy to overestimate the ultimate failure strength. In addition, the calculation of the debris flow intensity is based on the maximum flow velocity and flow depth, which suggests that the curve-derived intensity values are greater than the actual values (Chen et al., 2021). Owing to the limited number of data points, to increase the reliability of the vulnerability curves (Lee et al., 2024; Ettinger et al., 2016), more data on postfire debris flow events and validations are needed in the future. Finally, there is a need for a more detailed classification of damaged buildings with the assistance of a building damage database (Kang and Kim, 2016). This study mainly accounted for the development of vulnerability curves for BC buildings, not for other structural types. Compared with BC structures, RC frame buildings can resist a much greater impact pressure (Zhang et al., 2018). It is also necessary to consider mechanical failure criteria for unreinforced masonry walls of buildings in mountainous areas (Si et al., 2022). In addition, the building shape, direction, position, number of floors, building materials and construction codes in different regions were not accounted for (Lee et al., 2024; Wang et al., 2024). The need to consider the masking effects of the building complex resistance factor on debris flow movement is crucial in the future, as such effects can significantly reduce the destructive impact pressure on buildings located behind

https://doi.org/10.5194/egusphere-2025-772
Preprint. Discussion started: 11 June 2025

groups (Zhang et al., 2018). Addressing these factors in future research endeavours is crucial for increasing the comprehensiveness of vulnerability assessments (Wang et al., 2024). These limitations emphasize the need for further research to enhance the comprehensive management of hazard risks in mountainous rural areas.

5.2 Disaster reduction and emergency response suggestions

Both sides of Kule village are at risk of being impacted by the G1 and G2 gullies (Fig. 17). Owing to the impact of wildfires, there is a large amount of loose material in these gullies, which can trigger postfire debris flows again under low rainfall thresholds. Through the above field investigations and simulation predictions, debris flows can seriously damage buildings downstream of the alluvial fan and even block the Kule River, posing a severe threat to the lives of more than 300 people in the village. The most dangerous situation occurs when debris flows occur in the two gullies simultaneously (Fig. 17a). An immediate emergency response is crucial, and the escape route should be oriented along the vertical direction of the debris flow channel for reaching a safe location in high terrain (Fig. 17b). Left-bank residents should evacuate from both sides, thereby avoiding crossing the river. In contrast, right-bank residents should evacuate swiftly from the high-terrain area on their side. The safest suggestion is for residents to leave the village under feasible conditions. In the long term, reforestation can stabilize soil and reduce sediment into channels (Yang et al., 2022; Vahedifard et al., 2024). Thus, restoring vegetation in burned areas is essential for effectively suppressing postfire debris flows and promoting local ecological recovery (Yang et al., 2024).

https://doi.org/10.5194/egusphere-2025-772
Preprint. Discussion started: 11 June 2025

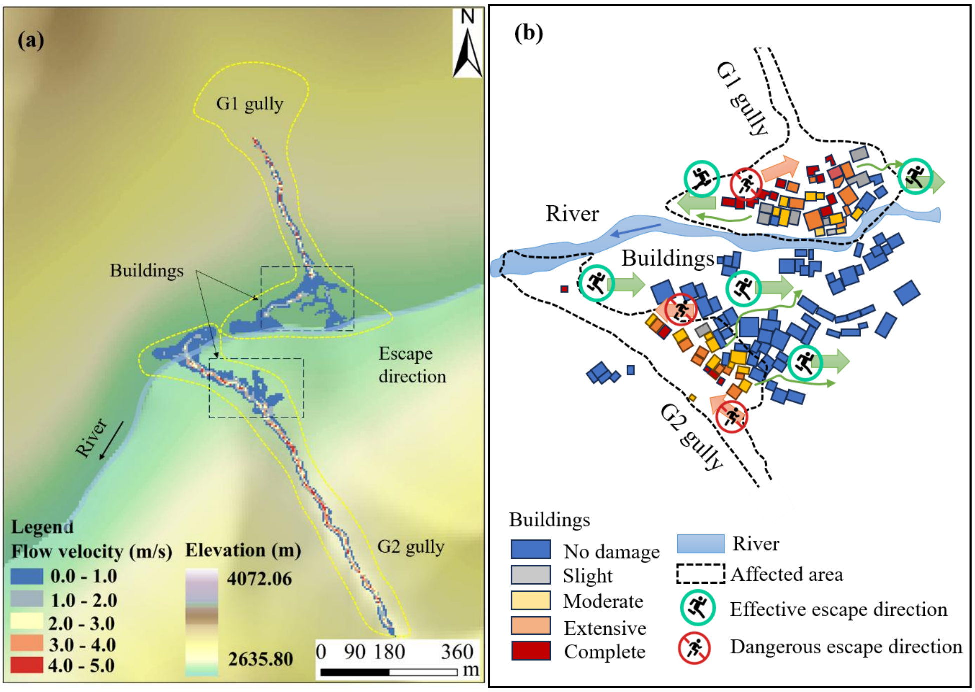

Figure 17 Disaster prediction and emergency response suggestions: (a) Simulation of debris flows occurring simultaneously in the G1 and G2 gullies; (b) emergency response and risk avoidance suggestions for the residents of Kule village.

6. Conclusions

This study focused on assessing the vulnerability of buildings to postfire debris flows in Kule village, Yajiang County. A physical vulnerability model for BC buildings was established to support the design of effective disaster management and emergency evacuation strategies for the region. The conclusions are as follows:

(1) A field investigation was conducted to analyse the characteristics of debris flows in the G1 and G2 gullies under the influence of wildfires and to document the damage features of 36 BC buildings in Kule village. The volume and peak discharge of postfire debris flows were

https://doi.org/10.5194/egusphere-2025-772
Preprint. Discussion started: 11 June 2025

calculated, and the damage degree of buildings was categorized using a range of vulnerability indices.

(2) Dynamic runout processes were simulated using the FLO-2D numerical model, with the reconstructed results calibrated to ensure consistency with actual situations. The simulations captured the debris flow intensities, including the flow depth, flow velocity, impact pressure, momentum flux, overturning moment, and relative burial height.

(3) Physical vulnerability curves for BC buildings damaged by postfire debris flows in the G1 gully were developed. The vulnerability model was subsequently applied to the G2 gully, which may also experience postfire debris flows, to predict potential building damage scenarios and their spatial distributions. Thus, emergency evacuation suggestions for Kule village were provided in the event of simultaneous debris flows in both gullies.

(4) The different vulnerability curves, intensity indicators, and function models were compared. Among the intensity indicators, the momentum flux was the most sensitive indicator for distinguishing damage categories. Conversely, the impact pressure could provide more accurate vulnerability values. Among the function models, the LNCDF function model demonstrated the highest statistical performance (MRE=0.09, PAF=1.09).

(5) The proposed vulnerability model exhibits certain limitations, emphasizing the importance of acknowledging and addressing the inherent uncertainty associated with various intensity indicators, function models, triggering and runoff mechanisms underlying postfire debris flows, and building structure and orientation.

Future research should focus on increasing the prediction accuracy and ensuring

https://doi.org/10.5194/egusphere-2025-772
Preprint. Discussion started: 11 June 2025

continuous, standardized postevent data collection processes, which will enhance the practical applicability of the developed vulnerability curves. Ultimately, this framework represents an important step towards developing physical vulnerability models, thereby providing comprehensive insights into the potential effects of future postfire debris flow events on buildings in similar regions and offering valuable guidance for formulating disaster management and mitigation strategies.

https://doi.org/10.5194/egusphere-2025-772
Preprint. Discussion started: 11 June 2025

Author contributions

JW: Writing - original draft, Methodology, Validation, Conceptualization. **JC**: Writing - Review & editing, Supervision, Funding acquisition. **LZ**: Investigation, Data curation. **FY**: Software. **XL**: Investigation. **WZ**: Resources. **HC**: Formal analysis.

Declaration of competing interest

The authors have no conflicts of interest to declare.

Acknowledgements

This study was supported by the National Key R&D Program of China (Grant No. 2024YFC3012705), the Nyingchi National Sustainable Development Experimental Zone Project (2023-SYQ-007), the National Natural Science Foundation of China (Grant No. 41925030) and the Science and Technology Research Program of the Institute of Mountain Hazards and Environment, Chinese Academy of Sciences (Grant No. IMHE-ZDRW-02).

Data availability

The authors agree to make data supporting the results or analyses presented in this paper available upon reasonable request to the first author and corresponding author.

https://doi.org/10.5194/egusphere-2025-772
Preprint. Discussion started: 11 June 2025

761 **Appendix A Debris flow intensities and building damage degree in G1 gully**

NO.	Flow depth (m)	Flow velocity (m/s)	Impact pressure (kPa)	Momentum flux (m^3/s^2)	Overturning moment (m^2/s)	Relative burial height	Damage degree
1	2.00	1.69	21.52	5.71	3.38	0.71	Complete
2	0.51	0.31	4.41	0.05	0.16	0.08	Slight
3	2.91	1.52	28.17	6.72	4.42	0.49	Complete
4	1.61	0.50	13.84	0.40	0.81	0.32	Extensive
5	1.98	1.05	18.37	2.18	2.08	0.36	Extensive
6	0.81	0.13	6.78	0.01	0.11	0.12	Slight
7	1.94	0.68	16.95	0.90	1.32	0.37	Extensive
8	1.61	0.85	14.64	1.16	1.37	0.27	Extensive
9	1.40	0.38	11.91	0.20	0.53	0.23	Moderate
10	2.20	1.35	21.42	4.01	2.97	0.29	Complete
11	1.51	0.87	13.87	1.14	1.31	0.30	Extensive
12	2.03	1.93	23.24	7.56	3.92	0.47	Complete
13	1.02	0.50	8.92	0.26	0.51	0.15	Moderate
14	1.21	0.44	10.41	0.23	0.53	0.18	Moderate
15	2.06	1.55	21.24	4.95	3.19	0.52	Complete
16	1.72	0.50	14.75	0.43	0.86	0.34	Extensive
17	2.08	1.32	20.29	3.62	2.75	0.42	Complete
18	0.61	0.19	5.14	0.02	0.12	0.12	Slight
19	1.25	0.48	10.80	0.29	0.60	0.21	Moderate
20	1.59	0.57	13.80	0.52	0.91	0.32	Extensive
21	0.83	0.39	7.17	0.13	0.32	0.18	Moderate
22	0.25	0.28	2.22	0.02	0.07	0.04	Slight
23	2.02	1.61	21.23	5.24	3.25	0.37	Complete
24	1.61	1.08	15.39	1.88	1.74	0.24	Extensive
25	1.24	0.42	10.63	0.22	0.52	0.18	Moderate
26	1.91	1.21	18.40	2.80	2.31	0.29	Extensive
27	1.17	0.37	9.98	0.16	0.43	0.15	Moderate
28	0.50	0.04	4.17	0.00	0.02	0.06	Slight
29	0.61	0.21	5.16	0.03	0.13	0.08	Slight
30	2.41	1.93	26.41	8.98	4.65	0.40	Complete
31	2.28	1.75	24.20	6.98	3.99	0.41	Complete
32	0.60	0.02	5.00	0.00	0.01	0.09	Slight
33	2.54	1.25	23.81	3.97	3.18	0.46	Complete
34	2.61	1.24	24.36	4.01	3.24	0.44	Complete
35	2.38	1.90	25.96	8.59	4.52	0.38	Complete
36	0.35	0.18	2.97	0.01	0.06	0.10	Slight

https://doi.org/10.5194/egusphere-2025-772
Preprint. Discussion started: 11 June 2025

Appendix B Debris flow intensities and predicted building counts in G2 gully: (a) Design frequency P=1%; (b) Design frequency P=1%

(a) Design frequency P=1%

NO.	Flow depth (m)	Flow velocity (m/s)	Impact pressure (kPa)	Momentum flux (m^3/s^2)	Overturning moment (m^2/s)	Relative burial height	Damage degree
1	2.30	0.69	19.97	1.10	1.59	0.38	Extensive
2	1.79	0.31	15.07	0.17	0.55	0.29	Moderate
3	1.90	0.67	16.59	0.85	1.27	0.42	Extensive
4	1.77	0.31	14.91	0.17	0.55	0.30	Moderate
5	1.15	0.50	10.00	0.29	0.58	0.21	Moderate
6	1.69	0.24	14.18	0.10	0.41	0.26	Moderate
7	2.54	0.67	21.92	1.14	1.70	0.39	Extensive
8	2.50	0.68	21.61	1.16	1.70	0.42	Extensive
9	3.50	2.00	35.96	14.00	7.00	0.58	Complete
10	3.10	1.80	31.33	10.04	5.58	0.69	Complete
11	2.96	1.18	27.02	4.12	3.49	0.66	Complete
12	1.60	0.50	13.75	0.40	0.80	0.21	Moderate
13	2.50	1.12	22.96	3.14	2.80	0.42	Extensive
14	2.00	0.80	17.75	1.28	1.60	0.44	Extensive
15	1.70	0.32	14.34	0.17	0.54	0.28	Moderate
16	1.51	0.29	12.72	0.13	0.44	0.23	Moderate
17	1.00	0.20	8.40	0.04	0.20	0.14	Slight
18	2.23	1.10	20.63	2.70	2.45	0.45	Extensive
19	1.44	0.65	12.71	0.61	0.94	0.29	Moderate
20	3.27	2.36	36.71	18.21	7.72	0.65	Complete
21	2.50	0.95	22.36	2.26	2.38	0.42	Extensive
22	1.78	0.45	15.17	0.36	0.80	0.30	Moderate
23	3.15	1.60	30.59	8.06	5.04	0.70	Complete
24	1.21	0.40	10.35	0.19	0.48	0.20	Moderate

https://doi.org/10.5194/egusphere-2025-772
Preprint. Discussion started: 11 June 2025

770 (b) Design frequency P=2%

NO.	Flow depth (m)	Flow velocity (m/s)	Impact pressure (kPa)	Momentum flux (m^3/s^2)	Overturning moment (m^2/s)	Relative burial height	Damage degree
1	1.70	0.44	14.49	0.33	0.75	0.28	Moderate
2	1.72	0.30	14.48	0.15	0.52	0.28	Moderate
3	1.35	0.31	11.41	0.13	0.42	0.30	Moderate
4	1.76	0.30	14.81	0.16	0.53	0.29	Moderate
5	0.90	0.20	7.57	0.04	0.18	0.16	Slight
6	1.62	0.33	13.68	0.18	0.53	0.25	Moderate
7	2.40	0.66	20.73	1.05	1.58	0.37	Extensive
8	1.80	0.45	15.34	0.36	0.81	0.30	Moderate
9	2.90	1.88	30.17	10.25	5.45	0.48	Complete
10	2.00	0.84	17.86	1.41	1.68	0.44	Extensive
11	2.75	1.25	25.56	4.30	3.44	0.61	Complete
12	1.07	0.30	9.07	0.10	0.32	0.14	Slight
13	2.45	0.95	21.94	2.21	2.33	0.41	Extensive
14	1.15	0.32	9.75	0.12	0.37	0.26	Moderate
15	1.50	0.38	12.74	0.22	0.57	0.25	Moderate
16	1.44	0.30	12.15	0.13	0.43	0.22	Moderate
17	1.22	0.11	10.18	0.01	0.13	0.17	Slight
18	1.50	0.50	12.92	0.38	0.75	0.30	Moderate
19	1.40	0.49	12.07	0.34	0.69	0.28	Moderate
20	2.80	2.30	32.32	14.81	6.44	0.56	Complete
21	2.34	0.85	20.72	1.69	1.99	0.39	Extensive
22	1.70	0.45	14.51	0.34	0.77	0.28	Moderate
23	3.00	1.30	27.86	5.07	3.90	0.67	Complete
24	1.00	0.30	8.48	0.09	0.30	0.17	Slight

771

https://doi.org/10.5194/egusphere-2025-772
Preprint. Discussion started: 11 June 2025

References

Barnhart, K. R., Miller, C. R., Rengers, F. K., & Kean, J. W. (2024). Evaluation of debris-flow building damage forecasts. Natural Hazards and Earth System Sciences, 24(4), 1459-1483.

Chang, M., Liu, Y., Zhou, C., & Che, H. (2020). Hazard assessment of a catastrophic mine waste debris flow of Hou Gully, Shimian, China. Engineering Geology, 275, 105733.

Chen, M., Tang, C., Zhang, X., Xiong, J., Chang, M., Shi, Q., ... & Li, M. (2021). Quantitative assessment of physical fragility of buildings to the debris flow on 20 August 2019 in the Cutou gully, Wenchuan, southwestern China. Engineering Geology, 293, 106319.

Chen, Y., Wang, Y., Zhang, X., Zhao, M., Zhou, Q., & Liu, T. (2025). Building risk amplification effect under loess landslides-hydraulic erosion-debris flow cascade in China. International Journal of Disaster Risk Reduction, 116, 105061.

Cui, P., Guo, X., Yan, Y., Li, Y., & Ge, Y. (2018). Real-time observation of an active debris flow watershed in the Wenchuan Earthquake area. Geomorphology, 321, 153-166.

Cui, P., Hu, K., Zhuang, J., Yang, Y., & Zhang, J. (2011). Prediction of debris-flow danger area by combining hydrological and inundation simulation methods. Journal of Mountain Science, 8, 1-9.

Cui, W. R., Chen, J. G., Chen, X. Q., Tang, J. B., & Jin, K. (2023). Debris flow characteristics of the compound channels with vegetated floodplains. Science of The Total Environment, 868, 161586.

Eidsvig, U. M. K., Papathoma-Köhle, M., Du, J., Glade, T., & Vangelsten, B. V. (2014). Quantification of model uncertainty in debris flow vulnerability assessment. Engineering

https://doi.org/10.5194/egusphere-2025-772
Preprint. Discussion started: 11 June 2025

Geology, 181, 15-26.

Ettinger, S., Mounaud, L., Magill, C., Yao-Lafourcade, A. F., Thouret, J. C., Manville, V., ... & Llerena, N. M. (2016). Building vulnerability to hydro-geomorphic hazards: Estimating damage probability from qualitative vulnerability assessment using logistic regression. Journal of Hydrology, 541, 563-581.

Fuchs, S., Heiss, K., & Hübl, J. J. N. H. (2007). Towards an empirical vulnerability function for use in debris flow risk assessment. Natural Hazards and Earth System Sciences, 7(5), 495-506.

Fuchs, S., Keiler, M., Ortlepp, R., Schinke, R., & Papathoma-Köhle, M. (2019). Recent advances in vulnerability assessment for the built environment exposed to torrential hazards: Challenges and the way forward. Journal of hydrology, 575, 587-595.

Gartner, J. E., Cannon, S. H., & Santi, P. M. (2014). Empirical models for predicting volumes of sediment deposited by debris flows and sediment-laden floods in the transverse ranges of southern California. Engineering Geology, 176, 45-56.

Gorr, A., McGuire, L., & Youberg, A. (2024). Empirical models for postfire debris-flow volume in the southwest United States. Journal of Geophysical Research: Earth Surface, 129(11), e2024JF007825.

Guo, X., Hürlimann, M., Cui, P., Chen, X., & Li, Y. (2024). Monitoring cases of rainfall-induced debris flows in China. Landslides, 21(10), 2447-2466.

He, K., Hu, X., Wu, Z., Zhong, Y., Zhou, Y., Gong, X., & Luo, G. (2024). Preliminary analysis of the wildfire on March 15, 2024, and the following post-fire debris flows in Yajiang

https://doi.org/10.5194/egusphere-2025-772
Preprint. Discussion started: 11 June 2025

County, Sichuan, China. Landslides, 21(12), 3179-3189.

Hu, K. H., Cui, P., & Zhang, J. Q. (2012). Characteristics of damage to buildings by debris flows on 7 August 2010 in Zhouqu, Western China. Natural Hazards and Earth System Sciences, 12(7), 2209-2217.

Jakob, M., Stein, D., & Ulmi, M. (2012). Vulnerability of buildings to debris flow impact. Natural hazards, 60, 241-261.

Kang, H. S., & Kim, Y. T. (2016). The physical vulnerability of different types of building structure to debris flow events. Natural Hazards, 80, 1475-1493.

Kean, J. W., Staley, D. M., Lancaster, J. T., Rengers, F. K., Swanson, B. J., Coe, J. A., ... & Lindsay, D. N. (2019). Inundation, flow dynamics, and damage in the 9 January 2018 Montecito debris-flow event, California, USA: Opportunities and challenges for post-wildfire risk assessment. Geosphere, 15(4), 1140-1163.

Lee, J. S., Song, C. H., Pradhan, A. M. S., Ha, Y. S., & Kim, Y. T. (2024). Development of structural type-based physical vulnerability curves to debris flow using numerical analysis and regression model. International Journal of Disaster Risk Reduction, 106, 104431.

Luo, H. Y., Zhang, L. M., Zhang, L. L., He, J., & Yin, K. S. (2023). Vulnerability of buildings to landslides: The state of the art and future needs. Earth-Science Reviews, 238, 104329.

Luo, H., Zhang, L., Wang, H., & He, J. (2020). Multi-hazard vulnerability of buildings to debris flows. Engineering Geology, 279, 105859.

Marchi L, Arattano M, Deganutti AM (2002) Ten years of debris-flow monitoring in the Moscardo Torrent (Italian Alps). Geomorphology 46:1–17.

https://doi.org/10.5194/egusphere-2025-772
Preprint. Discussion started: 11 June 2025

McGuire, L. A., Ebel, B. A., Rengers, F. K., Vieira, D. C., & Nyman, P. (2024). Fire effects on geomorphic processes. Nature Reviews Earth & Environment, 1-18.

Navratil, O., Liébault, F., Bellot, H., Travaglini, E., Theule, J., Chambon, G., & Laigle, D. (2013). High-frequency monitoring of debris-flow propagation along the Réal Torrent, Southern French Prealps. Geomorphology, 201, 157-171.

Ouyang, C., Wang, Z., An, H., Liu, X., & Wang, D. (2019). An example of a hazard and risk assessment for debris flows—A case study of Niwan Gully, Wudu, China. Engineering Geology, 263, 105351.

Ouyang, C., Xiang, W., An, H., Wang, F., Yang, W., & Fan, J. (2023). Mechanistic Analysis and Numerical Simulation of the 2021 Post-Fire Debris Flow in Xiangjiao Catchment, China. Journal of Geophysical Research: Earth Surface, 128(1), e2022JF006846.

Papathoma-Köhle, M., Gems, B., Sturm, M., & Fuchs, S. (2017). Matrices, curves and indicators: A review of approaches to assess physical vulnerability to debris flows. Earth-Science Reviews, 171, 272-288.

Papathoma-Köhle, M., Schlögl, M., Dosser, L., Roesch, F., Borga, M., Erlicher, M., ... & Fuchs, S. (2022). Physical vulnerability to dynamic flooding: Vulnerability curves and vulnerability indices. Journal of Hydrology, 607, 127501.

Quan Luna, B., Blahut, J., Van Westen, C. J., Sterlacchini, S., Van Asch, T., & Akbas, S. O. (2011). The application of numerical debris flow modelling for the generation of physical vulnerability curves. Natural hazards and earth system sciences, 11(7), 2047-2060.

Rengers, F. K., McGuire, L. A., Barnhart, K. R., Youberg, A. M., Cadol, D., Gorr, A. N., ... &

https://doi.org/10.5194/egusphere-2025-772
Preprint. Discussion started: 11 June 2025

Kean, J. W. (2023). The influence of large woody debris on post-wildfire debris flow sediment storage. Natural Hazards and Earth System Sciences, 23(6), 2075-2088.

Rengers, F. K., McGuire, L. A., Kean, J. W., Staley, D. M., & Hobley, D. E. J. (2016). Model simulations of flood and debris flow timing in steep catchments after wildfire. Water Resources Research, 52(8), 6041-6061.

Rickenmann D (1999) Empirical relationships for debris flows. Nat Hazards 19:47–77

Scheidl, C., & Rickenmann, D. (2010). Empirical prediction of debris-flow mobility and deposition on fans. Earth Surface Processes and Landforms: The Journal of the British Geomorphological Research Group, 35(2), 157-173.

Si, G. W., Chen, X. Q., Chen, J. G., Zhao, W. Y., Li, S., & Li, X. N. (2022). Failure criteria of unreinforced masonry walls of rural buildings under the impact of flash floods in mountainous regions. Journal of Mountain Science, 19(12), 3388-3406.

Sichuan Hydrological Manual (1984) Rainstorm-runoff calculation method in small watershed, 1984, Sichuan Water Conservancy and Power Department. Electronic publishing.

Thomas, M. A., Kean, J. W., McCoy, S. W., Lindsay, D. N., Kostelnik, J., Cavagnaro, D. B., ... & Collins, B. D. (2023). Postfire hydrologic response along the Central California (USA) coast: insights for the emergency assessment of postfire debris-flow hazards. Landslides, 20(11), 2421-2436.

Totschnig, R., Sedlacek, W., & Fuchs, S. (2011). A quantitative vulnerability function for fluvial sediment transport. Natural Hazards, 58, 681-703.

Vahedifard, F., Abdollahi, M., Leshchinsky, B. A., Stark, T. D., Sadegh, M., & AghaKouchak,

https://doi.org/10.5194/egusphere-2025-772
Preprint. Discussion started: 11 June 2025

A. (2024). Interdependencies between wildfire-induced alterations in soil properties, near-surface processes, and geohazards. Earth and Space Science, 11(2), e2023EA003498.

Wang, T., Chen, J., Chen, X., You, Y., & Cheng, N. (2018). Application of incomplete similarity theory to the estimation of the mean velocity of debris flows. Landslides, 15, 2083-2091.

Wang, T., Yin, K., Li, Y., Chen, L., Xiao, C., Zhu, H., & van Westen, C. (2024). Physical vulnerability curve construction and quantitative risk assessment of a typhoon-triggered debris flow via numerical simulation: A case study of Zhejiang Province, SE China. Landslides, 21(6), 1333-1352.

Yang, Y., Hu, X., Han, M., He, K., Liu, B., Jin, T., ... & Huang, J. (2022). Post-fire temporal trends in soil properties and revegetation: Insights from different wildfire severities in the Hengduan Mountains, Southwestern China. Catena, 213, 106160.

Yang, H., Liu, J., Sun, H., You, Y., Zhao, W., & Yang, D. (2024). Evolution characteristics of post-fire debris flow in Xiangjiao gully, Muli County. Catena, 246, 108353.

Zhang, B., Zhang, G., Fang, H., Wu, S., & Li, C. (2024). Risk assessment of flash flood under climate and land use and land cover change in Tianshan Mountains, China. International Journal of Disaster Risk Reduction, 115, 105019.

Zhang, S., Zhang, L., Li, X., & Xu, Q. (2018). Physical vulnerability models for assessing building damage by debris flows. Engineering Geology, 247, 145-158.

Zhou, B.F., Li, D.J., Luo, D.F., Lv, R.R., Yang, Q.X., 1991. Guide to Prevention of Debris Flow. Beijing, China.